Monthly Notices
of the
ROYAL ASTRONOMICAL SOCIETY

MNRAS **503,** 4601–4626 (2021)
Advance Access publication 2021 March 22

doi:10.1093/mnras/stab803

ALMA–IRDC: dense gas mass distribution from cloud to core scales

A. T. Barnes [1]★ J. D. Henshaw [2] F. Fontani [3,4] J. E. Pineda [3] G. Cosentino [5] J. C. Tan,[5,6] P. Caselli,[3] I. Jiménez-Serra,[7] C. Y. Law,[5] A. Avison [8,9] F. Bigiel,[1] S. Feng,[10,11,12] S. Kong,[13] S. N. Longmore,[14] L. Moser,[1] R. J. Parker [15]† Á. Sánchez-Monge[16] and K. Wang[17]

[1]*Argelander-Institut für Astronomie, Universität Bonn, Auf dem Hügel 71, D-53121 Bonn, Germany*
[2]*Max Planck Institute for Astronomy, Königstuhl 17, D-69117 Heidelberg, Germany*
[3]*Max-Planck-Institut für extraterrestrische Physik, Giessenbachstrasse 1, D-85748 Garching bei München, Germany*
[4]*INAF Osservatorio Astrofisico di Arcetri, Largo E. Fermi 5, I-50125 Florence, Italy*
[5]*Department of Space, Earth and Environment, Chalmers University of Technology, SE-412 96 Gothenburg, Sweden*
[6]*Department of Astronomy, University of Virginia, 530 McCormick Road Charlottesville, VA-22904-4325 USA*
[7]*Centro de Astrobiología (CSIC/INTA), Instituto Nacional de Técnica Aeroespacial, E-28850 Torrejón de Ardoz, Madrid, Spain*
[8]*UK ALMA Regional Centre Node, Jodrell Bank Centre for Astrophysics, School of Physics and Astronomy, The University of Manchester, Manchester M13 9PL, UK*
[9]*Jodrell Bank Centre for Astrophysics, Alan Turing Building, School of Physics and Astronomy, The University of Manchester, Manchester M13 9PL, UK*
[10]*National Astronomical Observatories, Chinese Academy of Science, Beijing 100101, People's Republic of China*
[11]*Academia Sinica Institute of Astronomy and Astrophysics, No.1, Section 4, Roosevelt Road, Taipei 10617, Taiwan, Republic of China*
[12]*National Astronomical Observatory of Japan, National Institutes of Natural Sciences, 2-21-1 Osawa, Mitaka, Tokyo 181-8588, Japan*
[13]*Steward Observatory, University of Arizona, Tucson, AZ 85719, USA*
[14]*Astrophysics Research Institute, Liverpool John Moores University, 146 Brownlow Hill, Liverpool L3 5RF, UK*
[15]*Department of Physics and Astronomy, The University of Sheffield, Hicks Building, Hounsfield Road, Sheffield S3 7RH, UK*
[16]*I. Physikalisches Institut, Universität zu Köln, Zülpicher Str 77, D-50937 Köln, Germany*
[17]*Kavli Institute for Astronomy and Astrophysics, Peking University, 5 Yiheyuan Road, Haidian District, Beijing 100871, China*

Accepted 2021 March 6. Received 2021 February 12; in original form 2020 October 9

ABSTRACT

Infrared dark clouds (IRDCs) are potential hosts of the elusive early phases of high mass star formation (HMSF). Here, we conduct an in-depth analysis of the fragmentation properties of a sample of 10 IRDCs, which have been highlighted as some of the best candidates to study HMSF within the Milky Way. To do so, we have obtained a set of large mosaics covering these IRDCs with Atacama Large Millimeter/submillimeter Array (ALMA) at Band 3 (or 3 mm). These observations have a high angular resolution (∼3 arcsec; ∼0.05 pc), and high continuum and spectral line sensitivity (∼0.15 mJy beam^{-1} and ∼0.2 K per 0.1 km s^{-1} channel at the N_2H^+ $(1-0)$ transition). From the dust continuum emission, we identify 96 cores ranging from low to high mass ($M = 3.4{-}50.9\,M_\odot$) that are gravitationally bound ($\alpha_{\rm vir} = 0.3{-}1.3$) and which would require magnetic field strengths of $B = 0.3{-}1.0$ mG to be in virial equilibrium. We combine these results with a homogenized catalogue of literature cores to recover the hierarchical structure within these clouds over four orders of magnitude in spatial scale (0.01–10 pc). Using supplementary observations at an even higher angular resolution, we find that the smallest fragments (<0.02 pc) within this hierarchy do not currently have the mass and/or the density required to form high-mass stars. None the less, the new ALMA observations presented in this paper have facilitated the identification of 19 (6 quiescent and 13 star-forming) cores that retain $>16\,M_\odot$ without further fragmentation. These high-mass cores contain trans-sonic non-thermal motions, are kinematically sub-virial, and require moderate magnetic field strengths for support against collapse. The identification of these potential sites of HMSF represents a key step in allowing us to test the predictions from high-mass star and cluster formation theories.

Key words: stars: formation – stars: massive – ISM: clouds.

1 INTRODUCTION

High-mass ($>8\,M_\odot$) stars are of great astrophysical importance due to the large amounts of energy and momentum, along with the production of heavy elements, that they inject into the interstellar medium (ISM) throughout their short lifetimes (Zinnecker & Yorke 2007). The later evolutionary stages, once the massive star has formed, have been well studied, and their role in driving the evolution of their host environment, and even the host galaxy, is relatively well understood. However, despite ongoing efforts, the earliest evolutionary stages, during the formation process of these massive stars, are not nearly as well constrained (e.g. Tan et al. 2014; Motte,

★ E-mail: ashleybarnes.astro@gmail.com
† Royal Society Dorothy Hodgkin Fellow.

Table 1. Table of the global properties across the cloud sample. Shown in columns are the cloud names from Butler & Tan (2012), IDs from Rathborne et al. (2006), the systemic velocity (v_{sys}), cloud kinematic distances (D_{cl}), effective radii ($R_{eff,\,cl}$), masses determined from near- and mid- infrared extinction mapping (M_{cl}), velocity dispersions from ^{13}CO (1 − 0) emission (σ_{cl}), virial parameters ($\alpha_{vir,\,cl}$), have all been taken from Kainulainen & Tan (2013, table 1). Also given is the mean *Herschel* derived dust temperature measured over the ALMA coverage ($T_{dust,\,cl}$), the non-thermal velocity dispersion and sonic Mach number ($\sigma_{NT,\,cl}$ and $\mathcal{M}_{NT,cl}$; Section 3.3), and the number of cores identified in the ALMA continuum observations (Section 3.1).

Cloud	ID 'G(longitude; latitude)'	v_{sys} (km s^{-1})	D_{cl} (pc)	$R_{eff,\,cl}$ (pc)	M_{cl} ($M_\odot$)	σ_{cl} (km s^{-1})	$\alpha_{vir,\,cl}$ –	$T_{dust,\,cl}$ (K)	$\sigma_{NT,\,cl}$ (km s^{-1})	$\mathcal{M}_{NT,cl}$ –	n_c #
Cloud A	G018.82-00.28	59–69	4800	10.4	18 500.0	2.04	1.4	18.3	2.0	7.9	8
Cloud B	G019.27 + 00.07	22–32	2400	2.71	2200.0	1.6	2.2	17.8	1.6	6.3	10
Cloud C	G028.37 + 00.07	73–83	5000	15.4	53 200.0	3.72	2.4	17.7	3.7	14.8	16
Cloud D	G028.53-00.25	81–91	5700	16.9	74 300.0	1.85	0.5	16.9	1.8	7.5	16
Cloud E	G028.67 + 00.13	75–85	5100	11.5	28 700.0	4.32	1.1	19.1	4.3	16.5	4
Cloud F	G034.43 + 00.24	52–62	3700.0	3.5	4460.0	3.62	1.3	20.0	3.6	13.5	20
Cloud G	G034.77-00.55	35–45	2900	3.06	3300.0	3.28	4.7	19.8	3.3	12.3	0
Cloud H	G035.39-00.33	38–48	2900	9.69	16 700.0	2.03	0.7	19.5	2.0	7.6	10
Cloud I	G038.95-00.47	38–48	2700	3.73	2700.0	1.65	1.2	18.0	1.6	6.4	9
Cloud J	G053.11 + 00.05	17–27	1800	0.755	200.0	0.96	1.5	19.0	0.9	3.5	3

Bontemps & Louvet 2018). Studies of the initial conditions of high-mass star-forming regions are required to unveil their formation mechanisms, before the disruptive effects of protostellar feedback disperse molecular clouds on a short time-scale (e.g. Kruijssen et al. 2019; Barnes et al. 2020b; Chevance et al. 2020a,b). This, however, first necessitates the identification of molecular clouds with sufficient mass and density, which currently exhibit a low star formation activity.

Infrared dark clouds (IRDCs) are a group of molecular clouds, the massive of which present promising candidates to study these initial conditions of high mass star formation (HMSF). These were initially identified with the *Infrared Space Observatory* (15 μm; Pérault et al. 1996) and the *Mid-course Space Experiment* (7 μm; Egan et al. 1998) as regions of strong mid-infrared extinction against the background Galactic emission, highlighting that they must contain substantial dust column densities. Subsequent work found that IRDCs can be cold (<20 K; Pillai et al. 2006; Ragan, Bergin & Wilner 2011), high mass ($\sim 10^{3-5}$ $M_\odot$; Rathborne, Jackson & Simon 2006; Longmore et al. 2012; Kainulainen & Tan 2013), have large column densities [$N(H_2) \sim 10^{22-25}$ cm^{-2}; Egan et al. 1998; Carey et al. 1998; Simon et al. 2006a; Vasyunina et al. 2009], and have high mean number densities [$n(H_2) \sim 10^{3-5}$cm^{-3}; e.g. Peretto et al. 2010; Peretto & Fuller 2010; Hernandez et al. 2011; Butler & Tan 2012]. Of particular importance, IRDCs can contain large reservoirs of relatively pristine gas, which has not been influenced by star formation, as inferred from their chemical composition (e.g. Miettinen, Hennemann & Linz 2011; Gerner et al. 2015; Barnes et al. 2016; Kong et al. 2016).

This is the first in a series of papers, which aims to conduct an in-depth assessment of the initial physical, chemical, and kinematic conditions for massive star/cluster formation across a sample of IRDCs using a suite of recently obtained Atacama Large Millimeter/submillimeter Array (ALMA) observations. The 10 cloud sample has been singled out by the stringent selection process summarized below, as being particularly good candidates in which to study the initial conditions of massive star formation; see fig. 1 from Tan et al. (2014) for comparison of their properties to wider molecular cloud population. First, the cloud sample was initially identified along with ∼11 000 other candidate IRDCs in the study of Simon et al. (2006a), which showed extended structure silhouetted against diffuse background emission. Simon et al. (2006b) then investigated the global properties of a sub-sample of these ∼11 000 clouds that were extended, had high extinctions, and were covered by the Galactic Ring Survey [a survey of ^{13}CO (1 − 0) molecular line emission; Jackson et al. 2006]. Rathborne et al. (2006) then investigated the clump properties within 38 of these clouds, selecting those that had known kinematic distance estimates (Simon et al. 2006b). Finally, Butler & Tan (2009, 2012) and Kainulainen & Tan (2013) studied the near- and mid-infrared extinction properties within 10 clouds of the Rathborne et al. (2006) sample, which were specifically chosen as being relatively nearby and massive. The properties of this cloud sample are given in Table 1. Fig. 1 shows a mid-infrared image covering ∼2° of the Galactic plane, where the positions of three clouds from our sample can be clearly seen as dark extinction features.

In this first paper, we investigate how the large, dense, and pristine mass reservoirs available within the cloud sample fragment down to the scales of individual (massive) star-forming cores (∼0.01 pc or ∼1000 au). This study is motivated by the need for observational constraints on the hierarchical mass distribution of IRDCs for testing the different theories of massive star formation. In many studies over the last decade, this was boiled down to differentiating between the predictions of core-accretion models (e.g. McKee & Tan 2003), where massive stars are born from the collapse of a massive core where small-scale fragmentation is suppressed, and competitive accretion models (e.g. Bonnell et al. 2001; Bonnell, Vine & Bate 2004), where the gas is highly fragmented into many thermal Jeans mass cores that form low-mass protostars, which then competitively accrete from the host clump environment. Although other theories have emerged more recently (e.g. Vázquez-Semadeni et al. 2019; Padoan et al. 2020), this paper provides the first in a suite of observational tests that aim at differentiating between these various prescriptions for HMSF.

This work is organized as the following. In Section 2, we give details of the ALMA observations of the 3 mm dust continuum and the N_2H^+ (1 − 0) line transition, which is thought to trace cold and dense molecular gas (e.g. Kauffmann et al. 2017; Pety et al. 2017; Barnes et al. 2020a). The results of the core identification and the calculation of their physical and dynamical properties are presented in Section 3. In Section 4, we outline the procedure used to create the homogenized literature core catalogue, where the same set of physical assumptions is used to recalculate previously published radio continuum core catalogues covering our cloud sample. This homogenized core catalogue is then analysed and compared to various scaling relations. Moreover, in Section 4, we link cores

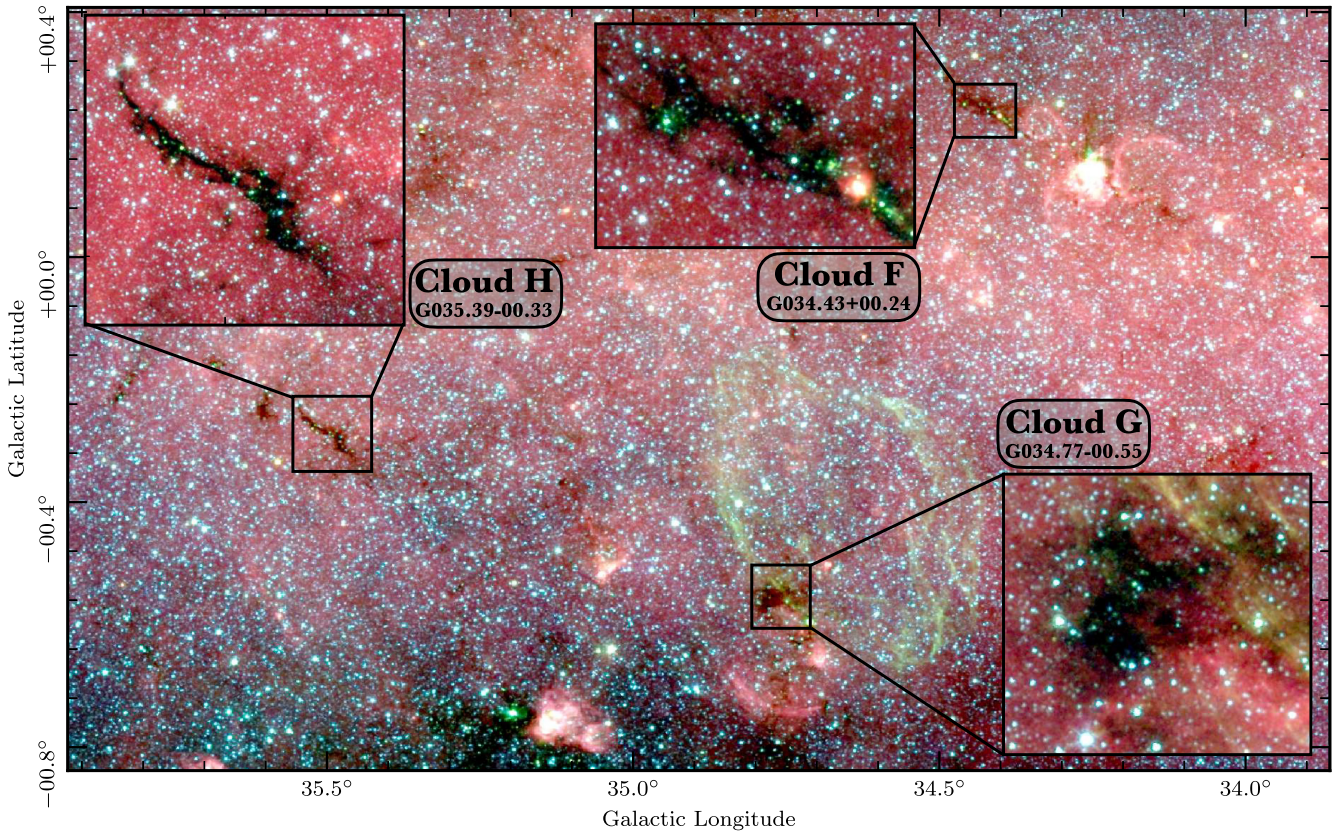

Figure 1. A three colour image of the Galactic plane where several infrared dark clouds (IRDCs) can be seen as dark extinction features. In this image, red is 8 μm, green is 5.8 μm, and blue is 4.5 μm emission from the *Spitzer* GLIMPSE survey (Carey et al. 2009). Labelled are three IRDCs that are investigated within this work: Clouds F, G, and H (or G034.43 + 00.24, G034.77-00.55, G035.39-00.33). The panels show zoom-ins of these IRDCs for more detail.

identified here to the cores from the literature catalogue, which allows us to identify several potential sites of HMSF, and follow the physical properties of the determined hierarchical structure from the cloud (∼1 pc) down to individual star-forming core scales (∼0.01 pc). This work is then summarized in Section 5. The appendix gives an example of the core and homogenized core catalogues, which can be found in full, machine-readable format online.

2 OBSERVATIONS

To investigate the dense gas properties within the IRDC sample, we have acquired high-angular resolution dust continuum and molecular line observations with ALMA as part of the projects: 2017.1.00687.S and 2018.1.00850.S (PI: A.T. Barnes). The observations used the Band 3 receiver, which was configured to obtain high spectral resolution observations (0.1 km s^{-1} or 30.518 kHz) of N_2H^+ (1 − 0) centred at ∼93 GHz, and a broad continuum bandwidth of ∼4 GHz. Complementary observations were made in the C43-1 12 m array configuration (baselines of 15–314 m) and 7 m (ACA) array (baselines of 8–48 m). Single dish total power observations were also performed for the molecular lines. This observational set-up was chosen to be directly comparable to the Plateau de Bure interferometer (NOEMA precursor) observations of the northern portion of one of the clouds in the sample (Cloud H; Henshaw et al. 2014, 2016a).

The 12 m and 7 m array observations were reduced and imaged by the CASA-PIPELINE (version: 5.4.0-70). In this work, we wish to make a direct comparison between the continuum and molecular line emission, and, hence, only use the 12 and 7 m observations that are available for both spectral configurations. The mosaic images from these arrays were combined with the FEATHER function in CASA (version 4.7.0; McMullin et al. 2007) with the default parameter set (i.e. effective dish size, single-dish scaling, and low-pass filtering of the single-dish observations). We present an in-depth analysis of the 12 and 7 m combination using the FEATHER function in Appendix B (see Figs B1 and B2), and deem this method to be accurate to within the underlying systematic uncertainties on the properties calculated within this work. The maximum recoverable scale within the combined images is set by the size of the smallest 7 m baseline of 8 m or 70 arcsec at 93.2 GHz. The average angular beam size achieved within the combined observations for both the continuum and molecular line observations is 2.9 arcsec, which, across the sample with distances ranging 1.8−5.7 kpc, is equivalent to a projected length-scale range of 0.05−0.1 pc.

The average continuum (4 GHz bandwidth) sensitivity achieved within the combined images with and without primary beam correction is 0.08 and 0.15 mJy beam^{-1}, respectively. We quote both here as the continuum images without primary beam correction are used later in this work in the source identification routine, whilst the images with primary beam correction are then used to measure core fluxes and any calculated physical properties. The corresponding mass sensitivity of the primary beam corrected image is ∼1 $M_\odot$ (assuming a dust temperature of 20 K; see equation 1). The average molecular line (30.518 kHz 0.1 km s^{-1} channel width) sensitivity is 15 mJy beam^{-1} or 0.2 K, which was chosen to allow a significant

Table 2. Table of the observational properties. Columned is the minor and major beam size, and mean rms value within the ALMA 3 mm continuum map and N_2H^+ (1 − 0) cube. The values of the mean continuum rms shown with and without parentheses have been determined using the maps with and without primary beam correction, respectively (see Section 3.1). The mean N_2H^+ (1 − 0) cube rms values have been determined within a 0.1 km s^{-1} channel.

Cloud	Continuum map			N_2H^+ cube		
	θ_{min} (arcsec)	θ_{maj} (arcsec)	rms (mJy beam^{-1})	θ_{min} (arcsec)	θ_{maj} (arcsec)	rms (K)
Cloud A	2.54	3.15	0.08 (0.16)	2.91	3.45	0.22
Cloud B	2.64	3.10	0.07 (0.14)	2.95	3.41	0.21
Cloud C	2.72	3.14	0.08 (0.16)	3.07	3.49	0.19
Cloud D	2.68	3.42	0.09 (0.18)	2.98	3.79	0.18
Cloud E	2.78	3.29	0.08 (0.17)	3.11	3.70	0.20
Cloud F	2.65	3.47	0.09 (0.19)	3.07	3.92	0.16
Cloud G	2.69	3.12	0.07 (0.15)	3.05	3.50	0.20
Cloud H	2.67	2.98	0.08 (0.16)	3.00	3.36	0.20
Cloud I	2.61	3.10	0.07 (0.16)	2.98	3.38	0.21
Cloud J	2.66	3.57	0.08 (0.19)	2.94	4.08	0.22

detection of the isolated hyperfine component of N_2H^+ (J, F_1, F = 1, 0, 1 → 0, 1, 2) across the sample (93.1762522 GHz; Caselli, Myers & Thaddeus 1995; Pagani, Daniel & Dubernet 2009).[1] The beam size and sensitivity information of the final continuum map, and N_2H^+ cube is presented in Table 2.

Ultimately, these observations allow us to accurately recover the dense 0.1 pc scale core population across a sample of IRDCs, and investigate their spatial distributions, and physical, kinematic, and chemical properties. An immediate follow-up work in the series of papers using the ALMA observations presented here, is the investigation of the $^{14}N/^{15}N$ fraction observed in N_2H^+ (Fontani et al. 2021).

3 RESULTS

The ALMA 3 mm dust continuum emission maps, and maps of the integrated intensity of N_2H^+ (1−0) are presented in Fig. 2 (second and third column, respectively). To produce the integrated intensity maps, we use cubes with a rest frequency centred on the isolated hyperfine component of N_2H^+ (1 − 0), and integrate emission between the systemic velocities shown in Table 1. In Fig. 2 (first column) we also show a three colour *Spitzer* GLIMPSE survey map, where the IRDCs can be seen as dark extinction features (Carey et al. 2009), and near- and mid-infrared extinction derived mass surface density maps (see fourth column; Kainulainen & Tan 2013). We find that a complex extended filamentary structure is present within the N_2H^+ (1 − 0) maps, which appears to be broadly similar to the structure for each cloud as seen in the infrared extinction observations. The continuum emission observations, on the other hand, appear much less extended. A comparison to the infrared images shows that the continuum maps recover only the extinction peaks, or infrared point sources (seen as the green sources in the three-colour image, and as holes in the mass surface density maps).

[1]The isolated hyperfine component is used to get an accurate measurement of the linewidth in the dynamical analysis of this work (Section 3.3), as, unlike the main hyperfine component, this is unlikely to merge with other hyperfine components and suffers from lower fractional optical depth (see e.g. Henshaw et al. 2014; Barnes et al. 2018).

3.1 Core identification

Despite the relatively simple morphology of the continuum emission, we characterize the structures present across the sample using a dendrogram analysis (Rosolowsky et al. 2008). The use of a structure-finding algorithm, as opposed to by-eye identification, is preferred to give reproducibility and allow a systematic comparison across the sample. Dendrogram analysis, in particular, was chosen to allow a more direct comparison to other works that cross-over with our cloud sample (Henshaw et al. 2016a, 2017; Liu et al. 2018b).

We run the dendrogram analysis using the combined 12 and 7 m array continuum maps that have not been corrected for the primary beam response. These maps have a flat noise profile, and therefore are preferred over the primary beam corrected maps, as the initial determination of the dendrogram structure relies on the constant noise threshold calculated for each cloud (see Table 2). We found that the use of the primary beam corrected maps typically caused the dendrogram algorithm to identify noise features towards the edge of the mapped region as significant structures. We tested a range of input parameters for the dendrogram analysis of the non-primary beam corrected maps, and found that a set of parameters similar to Liu et al. (2018b) produced the structure that best resembled what would be identified through manual inspection of the continuum maps. Along with allowing a more direct comparison to the Liu et al. (2018b) results, this parameter set has the benefit of being well tested for several additional data sets covering the same sources observed in this work (e.g. Henshaw et al. 2016a; Cheng et al. 2018). The set of parameters that are used for the determination of the dendrogram structure used throughout this work is MIN_VALUE = 3 σ = 0.24 mJy beam^{-1} (the minimum intensity considered in the analysis), MIN_DELTA = 1σ (the minimum spacing between isocontours), MIN_PIX = 0.5 beam area ∼18 pixels (the minimum number of pixels contained within a structure). We tested these parameters, and found that minor changes were required to achieve dendrogram hierarchies that include all structures identified from manual inspection of the continuum maps. It is worth keeping in mind that the choice of any parameter set in an automated structure identification algorithm only allows for a reproducible structure, and, ultimately, the user must check the results for inherently complex data sets.

Overlaid as coloured contours on the maps shown in Fig. 2 are the leaves identified from the dendrogram analysis. The leaves represent the highest level (smallest) structures in the dendrogram analysis, which we refer to as 'cores' within this work. The positions and effective radii ($R_{eff} = \sqrt{A/\pi}$, where A is the area enclosed within the dendrogram boundary) of the 96 identified cores can be found in Table A1. We find that around 5–15 cores are present within each cloud, with the exception of Cloud G where no cores have been identified. This was likely because the mapped region of Cloud G is, by design, focused on the eastern shocked region explored by Cosentino et al. (2018, 2019), and not the main dust extinction/continuum feature(s) previously identified within this cloud (e.g. Rathborne et al. 2006; Butler & Tan 2012; Kainulainen & Tan 2013).

Although the dendrogram structure itself has been calculated using the non-primary beam corrected continuum maps, all fluxes quoted in this work have been corrected for the primary beam response. Moreover, when determining the total primary beam corrected flux for each core, we consider that these are not isolated structures, but rather that they are sitting within the complex 3D geometry of their clouds. They therefore may have some foreground and background flux contribution from their host environment (Rosolowsky et al. 2008). We therefore follow two methods to determine the total flux within a given core boundary. The first assumes that there is

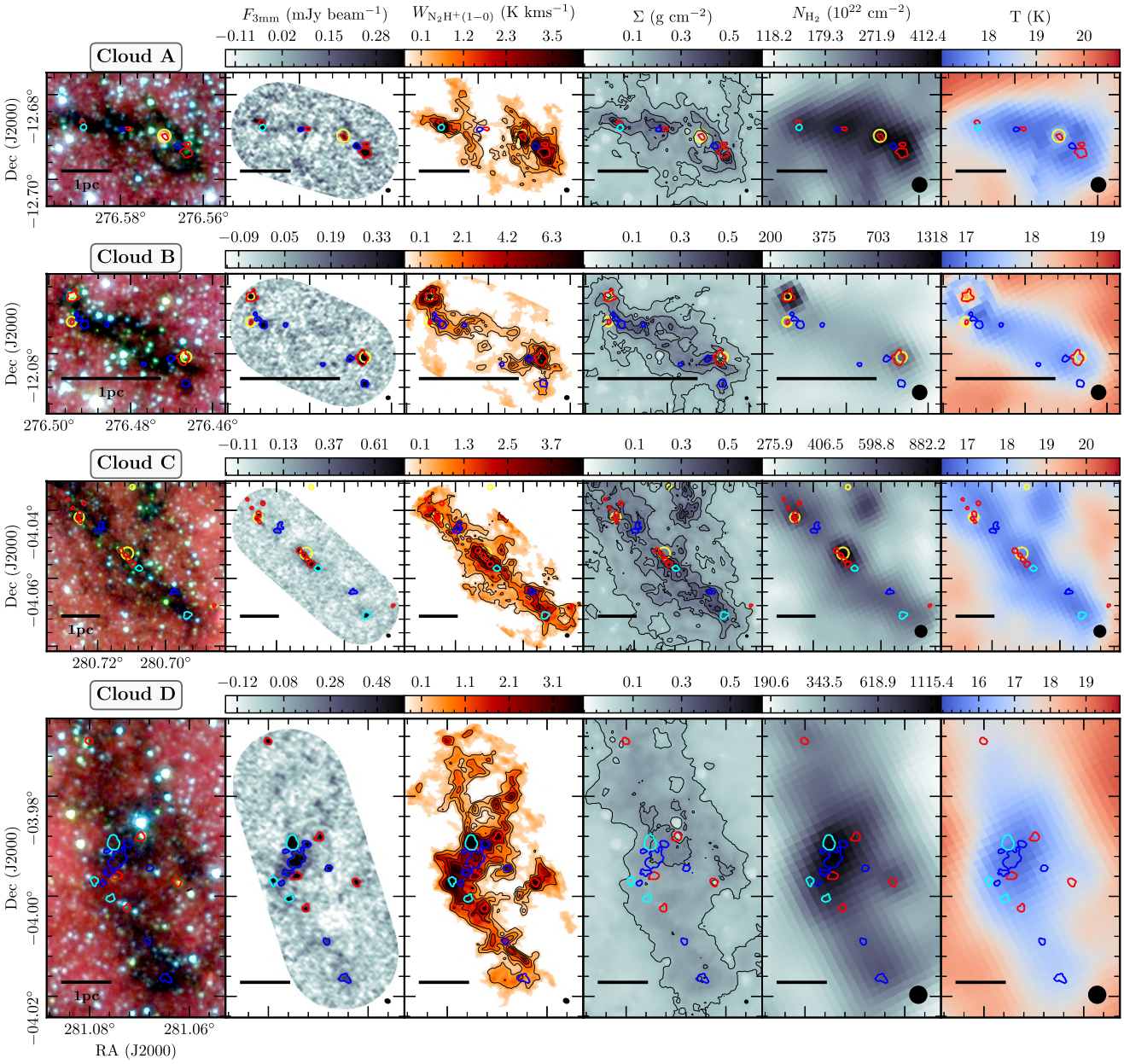

Figure 2. (first column) Three colour images from the *Spitzer* GLIMPSE survey (Churchwell et al. 2009). (second) The ALMA 3 mm dust continuum (without the primary beam correction), and (third) N_2H^+ (J,F_1,F = 1,0,1 → 0,1,2) integrated intensity maps. (fourth) Combined near- and mid-infrared extinction derived mass surface density maps (Kainulainen & Tan 2013). (fifth) Far-infrared *Herschel* derived column density, and (sixth) dust temperature maps (Marsh et al. 2016, 2017). The yellow circles overlaid on each panel show the positions and sizes of 70 μm emission point sources (Molinari et al. 2016; Marton et al. 2017). The coloured contours overlaid on each panel show boundaries of all the 'leaves' (or cores) identified using the dendrogram analysis on the dust continuum maps (see Section 3.1). The red and blue contours indicate the cores that have been classified as star forming and quiescent, respectively (Section 3.1). The cyan contours indicate the cores that have been identified as being quiescent, high mass, and without further fragmentation (see Section 4.3.2). Shown in the lower left of the ALMA observation panels is the beam size, and in the lower left of the three colour image (first panel) is a scale bar adjusted for the distance of each cloud (see Table 1).

no background contribution of the flux, which is that all of the flux within the leaf boundary is attributed to that structure (S_ν). The second approach is to assume that a core is superimposed on top of the background flux level, which needs to be subtracted to get the 'background subtracted flux' ($S_\nu^{\rm b}$). In practice, we take the structure that is directly below a given leaf in the dendrogram hierarchy as its background level (i.e. the branch where the leaf is located), and determine the background subtracted flux as the remaining flux after having subtracted the contribution of this lower level structure from the leaf (e.g. Pineda et al. 2015; Henshaw et al. 2016b). All properties determined within this work using this background-subtracted flux will be denoted by a superscript 'b' (e.g. $M^{\rm b}$ is the background-subtracted mass). We find that the total flux contribution from the leaves after subtraction of background emission is $S_\nu^{\rm b}/S_\nu = 0.29^{+0.23}_{-0.11}$.[2] These flux values are summarized in Table A1.

One of the primary aims of this work is to identify and study the earliest stages of HMSF. Therefore, finally, we determine if the cores

[2]For all statistics we present within this section, we show the median (50 percentile) of the sample distribution, and one standard deviation around this value (15.9 and 84.1 percentile).

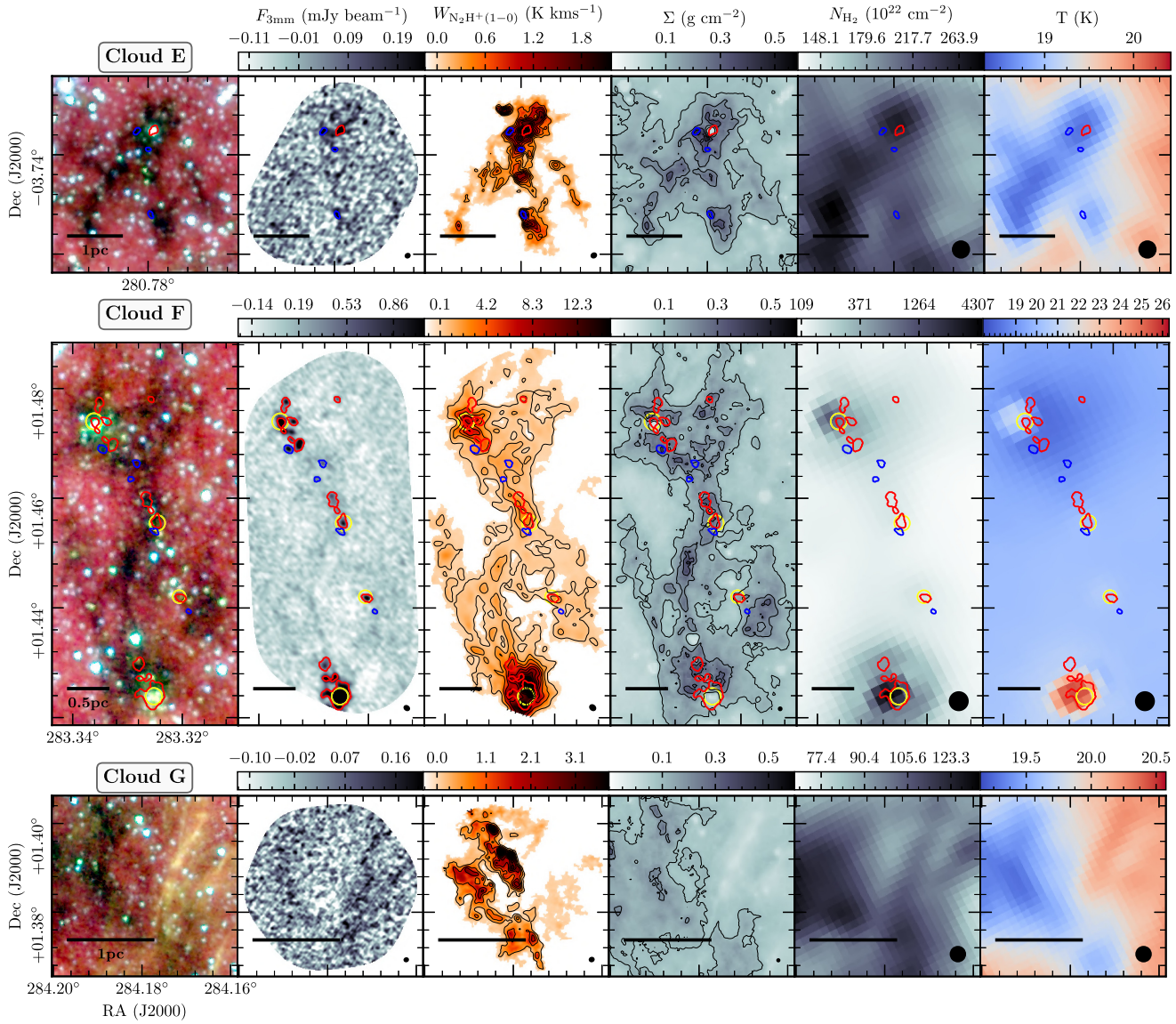

Figure 2. *continued.*

(i.e. dendrogram leaves) contain any near- or mid-infrared emission, which could be suggestive of them being at a later evolutionary stage and potentially harbouring active star formation (e.g. Ragan et al. 2012; Rigby et al. 2021). To do so, we compare the cores to the *Spitzer* 3.6 μm (blue), 4.5 μm (green), and 8 μm (red) three-colour images (Churchwell et al. 2009), as shown in Fig. 2 (first column). We then visually determined if there is an infrared point source within each of the core boundaries as defined by the dendrogram contours. These associations are then cross-referenced with the *Herschel* 70 μm emission maps and point source catalogue, also overlaid as circles in Fig. 2 (Molinari et al. 2016; Marton et al. 2017). We find that the majority of 70 μm point sources have corresponding *Spitzer* emission (∼90 per cent), yet many of the *Spitzer* emission sources do not have 70 μm emission (∼60 per cent). Sources containing either or both *Spitzer* emission or a 70 μm point source are labelled as star forming in our catalogue. This combination of infrared emission allows for a rigorous detection of both early and later stages of embedded star formation across our core sample. The star-forming state of each core is provided in Table A1. In Fig. 2, quiescent cores are represented by the blue and cyan contours (see Section 4.3.2 for a discussion of the cyan contours), and star-forming cores are represented by the red contours in Fig. 2.

3.2 Physical properties

In this section, we determine the physical properties of the core catalogue identified using the dendrogram analysis (Section 3.1). First, we determine the projected size (or effective radius) and masses of each core. We find an angular size distribution of $R_{\rm eff} = 2.4^{+0.8}_{-0.8}$ arcsec, which highlights that the majority of the cores have sizes only marginally larger than the mean beam radius of ∼ 1.5–2 arcsec, and therefore are not fully resolved (see Table 2). This angular size distribution corresponds to a projected size distribution of $R_{\rm eff} = 0.04^{+0.02}_{-0.02}$ pc (or 9210^{+4844}_{-4197} au), when accounting for the source distances given in Table 1. The uncertainty in $R_{\rm eff}$ from observational errors (e.g. pointing) is negligible compared to the uncertainty introduced from the kinematic distance. Simon et al.

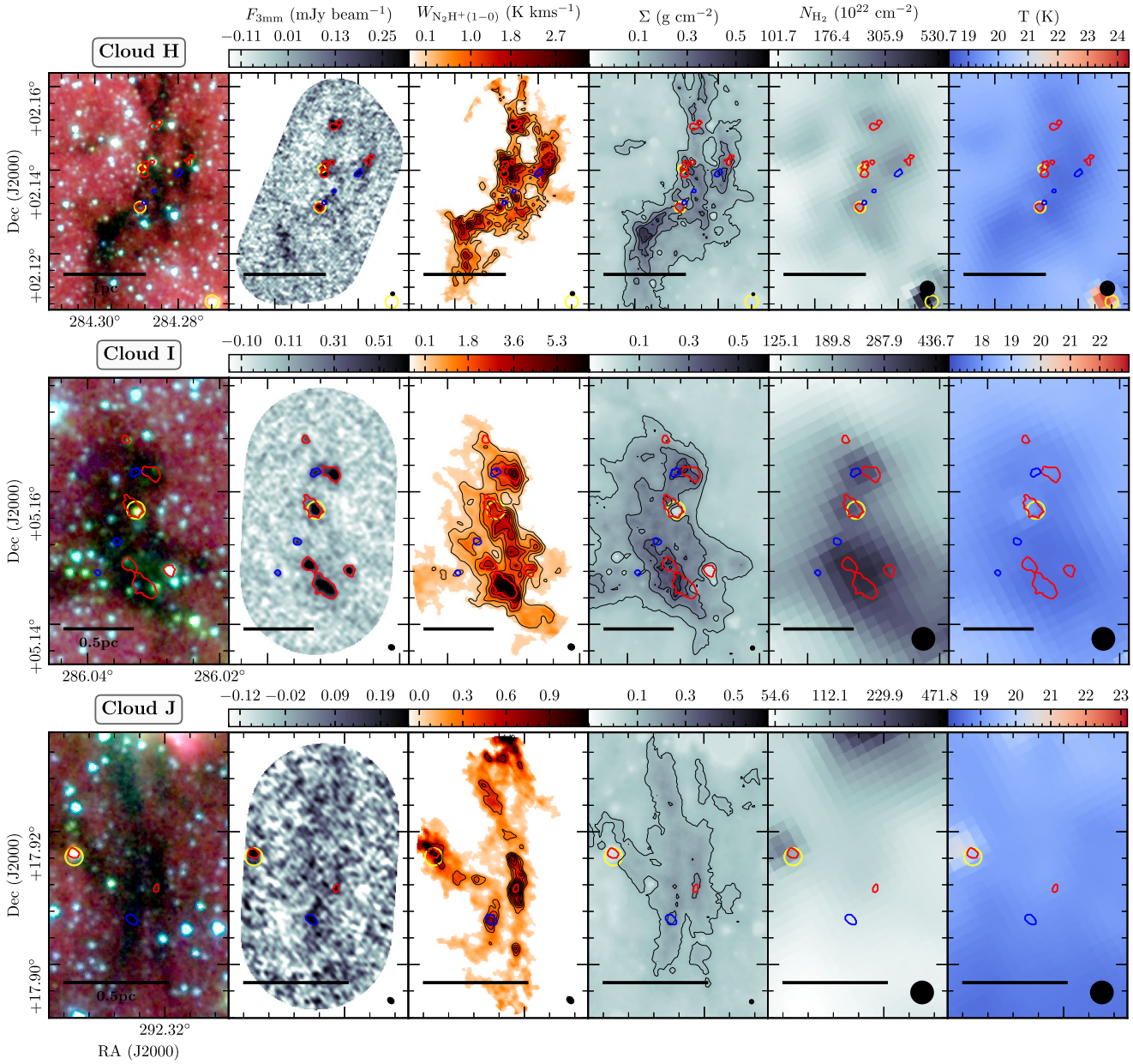

Figure 2. *continued.*

(2006b) estimated that the kinematic distances are typically accurate to ∼15 per cent, which we adopt for our uncertainty on the radius.

To calculate the mass of each core, we use the integrated flux (S_ν; see Table A1) following

$$M = \frac{d^2 S_\nu R_{\rm gd}}{\kappa_\nu B_\nu(T_{\rm dust})}, \quad (1)$$

where d is the source distance (see Table 1), $R_{\rm gd} = 141$ is the total (gas plus dust)-to-(refractory-component-)dust-mass ratio (assuming a typical interstellar composition of H, He, and metals; Draine 2011),[3] $B_\nu(T_{\rm dust})$ is the *Planck* function for a dust temperature, $T_{\rm dust}$, at a representative frequency of $\nu = 90.664$ GHz, and $\kappa_\nu = \kappa_0\,(\nu/\nu_0)^\beta \approx 0.175\,{\rm cm^2 g^{-1}}$, when assuming $\nu_0 = 230$ GHz, $\beta = 1.75$ (Battersby et al. 2011) and $\kappa_0 = 0.899\,{\rm cm^2\,g^{-1}}$ (Ossenkopf & Henning 1994 result for an MRN size distribution with thin ice mantles after 10^5 yr of coagulation at a density of 10^6 cm^{-3}).

To obtain an estimate of the dust temperature towards each of the cores, we use spectral energy distribution (SED) fits to the far-infrared dust continuum observed with *Herschel* (Hi-Gal; Molinari et al. 2016). We use the mean line of sight results from the PPMAP project shown in Fig. 2 (Marsh et al. 2016, 2017). To check the fidelity of the PPMAP column density and temperature maps, where possible, we compare to the corresponding maps from Nguyen Luong et al. (2011), Lim et al. (2016), Zhang et al. (2017), and Soam et al. (2019). These authors independently produced column density and temperature maps following a more conventional far-infrared SED-fitting routine, whilst accounting for the background

[3]Here, we adopt a higher than typically assumed value for the dust-to-gas ratio, which determined from $M_{\rm H}/M_{\rm dust} = 101$ (see table 21.3 of Draine 2011), or $M_{\rm total}/M_{\rm dust} = 1.4 \times 101 = 141$ (see table 1.4 of Draine 2011 for $M_{\rm total}/M_{\rm H} = 1.4$).

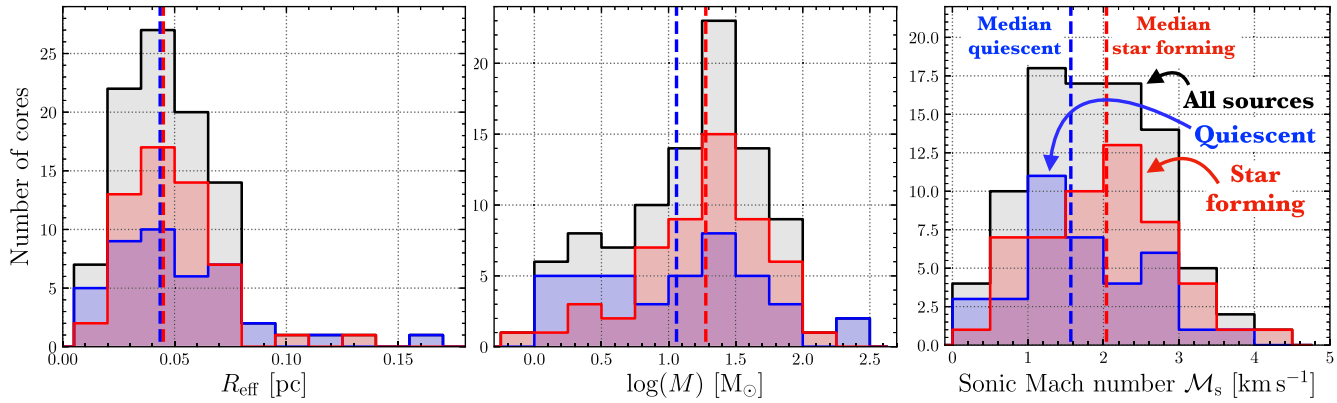

Figure 3. Distribution of the properties determined across the core sample (Section 3.3). Shown in panels from left to right is the effective radius ($R_{\rm eff}$), the (logarithm) mass (M), and sonic Mach number ($\mathcal{M}_{\rm s} = \sigma_{\rm NT}/\sigma_{\rm T}$) calculated across the core sample (Section 3.3). Shown as black, red, and blue stepped profiles are the histograms for the whole sample, the star-forming cores and quiescent (non-star forming) cores, respectively. The red and blue vertical dashed lines show the median values for the star-forming cores and quiescent cores.

in *Herschel* observations. We find broadly comparable values of both the column density and temperature within these conventional maps and the PPMAP maps, albeit the dust temperature determined with PPMAP appears to be a few degrees higher towards the cloud centres (also see Marsh et al. 2017 for a similar comparison). As this does not significantly affect the results of this paper, and because the PPMAP data set is the only available consistent set of maps for the full IRDC sample, for consistency we choose to use the PPMAP results (additional sources of uncertainty on, e.g. the dust temperature measurements are discussed throughout this work).

We find dust median temperatures of $T_{\rm dust} = 17.8^{+1.4}_{-0.9}$ K. These dust temperatures for each core are then used to calculate a median mass of $M = 18.4^{+32.5}_{-15.0}$ M$_\odot$ across the core sample ($M^{\rm b} = 4.6^{+16.8}_{-3.7}$ M$_\odot$).[4] We assumed a typically ∼10 per cent in the absolute flux scale of the ALMA observations, and, following Sanhueza et al. (2017), we assume an uncertainty of ∼30 per cent dust opacity. These uncertainties in the dust opacity, dust emission fluxes, and the distance propagate to give an uncertainty of ∼50 per cent in masses. The histogram distribution of the size and mass of the star-forming and quiescent core samples is shown in Fig. 3.

It is worth noting that the dust temperatures measured here are averages sampled by the beam of the PPMAP maps (∼12 arcsec; shown as a black circle in the rightmost panel of Fig. 2), and the beam of the ALMA observations used in this work is significantly smaller (∼3 arcsec; see Table 2). Therefore, smaller scale temperature variations due to, e.g. cold cores or embedded stellar objects could cause us to overestimate or underestimate the temperature, respectively (see e.g. Ragan et al. 2011; Dirienzo et al. 2015; Sokolov et al. 2017).

To quantify the extent that the cores containing embedded protostars may have underestimated temperatures in the PPMAP maps, we follow a procedure outlined in Peretto et al. (2020) for determining the temperature at higher angular resolution (∼5 arcsec). For this estimate, these authors require that the cores have an identified 70 μm point source (the 70 μm flux given in Table A1). The 70 μm flux is then converted to a bolometric flux following the relation from Elia et al. (2017), which is thought to apply to high-mass star-forming regions. Following flux conservation, this luminosity can then be converted to a temperature profile (Terebey, Chandler & Andre 1993). Using the same fiducial parameters as Peretto et al. (2020), we determine the mass-averaged temperature for each of our 70 μm cores. We find that temperature estimates from the 70 μm emission are systematically higher than those within the PPMAP. The mean difference in temperature is a factor of 50 per cent, which on average corresponds to 30 per cent lower 70 μm mass estimates, $M_{70\,\mu{\rm m}}$ (see Table A2). These differences are included as additional uncertainties for our star-forming sample, which propagate to a ∼60 per cent in their mass estimates from PPMAP that are adopted throughout this work.

We also obtain masses from the extinction derived mass surface density maps of the clouds (Kainulainen & Tan 2013; as shown in Fig. 2). These maps have a comparable angular resolution to our ALMA observations, and therefore should serve as an independent measure of the core masses. Extracting the extinction total mass within the core boundaries gives a median value of $M_{\rm ext} = 6.3^{+11.0}_{-4.7}$ M$_\odot$, which is a significant fraction below the continuum derived masses: $M_{\rm ext}/M = 0.5^{+0.4}_{-0.3}$. This offset was also noted by Henshaw et al. (2016a), who compared 3 mm dust continuum and extinction derived masses within the northern portion of Cloud H, not included in these observations. We assess if this could be a product of the artificially lower values within the mass surface density maps, where infrared point source emission inhibits an accurate extinction measurement (e.g Kainulainen et al. 2009; Butler & Tan 2009, 2012; Kainulainen & Tan 2013).[5] These can be seen by comparing the infrared three colour image and mass surface density maps within Fig. 2.

Fig. 4 shows the core masses determined from the near- and mid-infrared extinction as a function of the core masses determined from the 3 mm ALMA continuum, where cores with and without signs of star formation are shown in red and blue, respectively. Here, we see that the cores are systematically offset towards higher continuum determined masses by around a factor of 2 to 3 (compare to the black-dashed lines). Moreover, we see that the ratio of the

[4]We also determine the masses for a fixed temperature of 18 K, which approximately corresponds to the mean dust temperature determined across the cloud sample.

[5]We note that the mass surface density maps contain negative values towards the brightest infrared point sources. As a result of this, there are two cores associated with infrared point sources that have negative masses, which we remove from our sample when calculating the $M_{\rm ext}$ statistics.

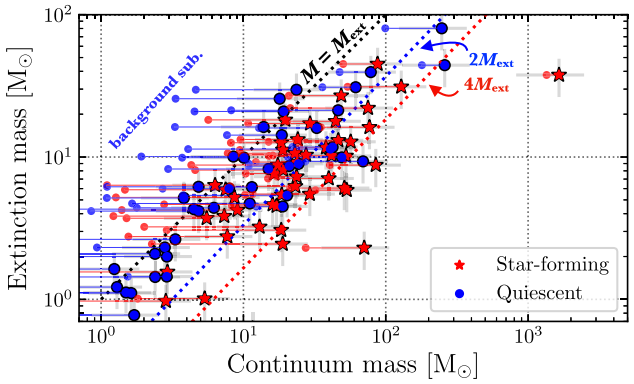

Figure 4. A comparison between the core masses determined from the 3 mm ALMA continuum and combined near- and mid-infrared extinction (Section 3.2). The cores classified as actively star forming or quiescent are shown in red and blue, respectively. Shown as points with and without a black outline are the mass estimates determined without and with background subtraction (see Table A2). We show the uncertainty ranges of ∼50 and ∼60 per cent for star-forming continuum mass estimates, respectively, and ∼30 per cent for the extinction masses estimates (Butler & Tan 2009, 2012; Kainulainen & Tan 2013). The diagonal dotted lines show the continuum and extinction determined masses are equal ($M = M_{\rm ext}$), and the continuum determined mass is a factor of 2 and 4 higher ($M = 2M_{\rm ext}$, $M = 4M_{\rm ext}$).

extinction to continuum mass estimates ($M_{\rm ext}/M$) with signs of star formation are systematically lower than those without star formation. We calculate that the median ratio with and without star formation is $M_{\rm ext}/M = 0.29$, $M_{\rm ext}/M = 0.68$, respectively. It is then reasonable to suggest that the larger difference for the cores with star formation is primarily a result of the extinction maps having lower values of the mass surface density towards bright infrared point sources (Butler & Tan 2009, 2012; Kainulainen et al. 2009; Kainulainen & Tan 2013; Butler, Tan & Kainulainen 2014). However, the remaining factor of 2 difference between the continuum and extinction determined masses for the non-star-forming sources is not clear (also see Henshaw et al. 2016b; Kong et al. 2018; Liu et al. 2018b).

In Fig. 4, we also show the background-subtracted continuum masses for reference. However, we note that the extinction derived masses have not been background subtracted. Hence, this is not direct comparison, and the inclusion of background subtraction cannot stand as an explanation for the remaining difference. Varying the assumed dust properties within reasonable limits cannot account for the factor of 4 difference in mass estimates for the quiescent sources. In addition, we note that the masses of the star-forming sources determined using the 70 μm temperature estimate are still systematically higher than the extinction based estimate ($M_{\rm ext}/M_{70\,\mu\rm m} = 0.35$). We then attribute this to the variety of systematic uncertainties inherent in the extinction mapping technique, which include foreground corrections that affect lower column density regions, and saturation effects at high optical depths that cause the mass in high mass surface density regions to be underestimated (Butler & Tan 2009, 2012; Kainulainen & Tan 2013; Butler et al. 2014).

The molecular hydrogen number density of each core is determined using

$$n_{\rm H_2} = \frac{M}{\frac{4}{3}\pi R_{\rm eff}^3 \mu_{\rm H_2} m_{\rm H}}, \tag{2}$$

where $\mu_{\rm H_2} = 2.8$ is the mean molecular weight per hydrogen molecule (Kauffmann et al. 2008), and $m_{\rm H}$ is the mass of a hydrogen atom. We find molecular hydrogen number densities across the sample of $n_{\rm H_2} = 6.9^{+5.6}_{-3.2} \times 10^5$ cm^{-3}, or when using the background-subtracted mass $n^{\rm b}_{\rm H_2} = 2.0^{+2.3}_{-1.2} \times 10^5$ cm^{-3}. The corresponding local free-fall time is calculated as

$$t_{\rm ff} = \left(\frac{\pi^2 R_{\rm eff}^3}{8GM}\right)^{0.5} = \left(\frac{3\pi}{32 G \mu_{\rm H_2} m_{\rm H} n_{\rm H_2}}\right)^{0.5}, \tag{3}$$

where G is the gravitational constant. We find local free-fall times across the sample of $t_{\rm ff} = 3.7^{+1.4}_{-1.0} \times 10^4$ yr. The number densities and free-fall times for each core are given in Table A2.

3.3 Dynamical properties

We now determine the core dynamical properties, which will be used later to assess the stability of the cores. We use the (1−0) transition of N_2H^+ to determine the line-of-sight velocity dispersion for each of the cores. To do so, we extract the average spectra from within the leaf contours.[6] We fit each of the spectra using the standalone fitter functionality of SCOUSEPY (Henshaw et al. 2019). This procedure uses a technique called derivative spectroscopy to provide an estimate of the number of emission features within each spectrum (Lindner et al. 2015; Riener et al. 2019). Briefly, this technique involves smoothing the spectrum using a Gaussian kernel. Features such as maxima, minima, and inflection points detected within the derivatives of this smoothed spectrum can be then used to determine estimates of the peak amplitude, centroid velocity, and width of each emission feature within a spectrum. SCOUSEPY feeds these values as free-parameter guides to PYSPECKIT (Ginsburg & Mirocha 2011), which performs the fitting. The size of the smoothing kernel is provided as an input parameter and is somewhat data dependent (Riener et al. 2019, use machine learning to determine this parameter), however, we set a value of either 3, 4, 5, or 6 for 1, 1, 59, and 35 cases, respectively. SCOUSEPY also allows for manual intervention. Manual fitting was performed in cases where the width of the main group of hyperfine components is such that the emission encroached within our fixed window around the isolated component, leading to the identification of peaks that we do not want to fit. We find that 47 of the 96 cores required multiple Gaussian components to accurately reproduce the observed spectra. The majority of these (38) required only an additional component, but we note that 9 cases had particularly complex spectra that required three components. In these cases with multiple velocity components, we assign the component with the largest integrated intensity to the core.

An example of a complex spectral profile observed towards core A1c3 is shown in Fig. 5. This spectrum has been decomposed into three velocity components by SCOUSEPY, which are shown as the purple, blue, and red-dashed, filled Gaussian profiles. The sum of these components is shown as a dashed grey profile, and the residual of the observed spectrum minus the total profile is shown as a solid black centred on −0.5 K. This residual profile contains variations at the level of the noise, which validates the choice of fitting parameters to accurately reconstruct the observed profile. Also shown in Fig. 5 are maps of the N_2H^+ (1−0) intensity integrated over the approximate velocity range covered by each component. These are shown with colour scales that match the colours used to show the Gaussian profiles. Overlaid as the black-dashed contours

[6]The spectra have been adjusted to a rest frequency of 93176.2522 MHz, corresponding to the isolated hyperfine component J, F_1, F = 1, 0, 1 → 0, 1, 2, from the original rest frequency of 93176.7637 MHz that corresponds to the brightest hyperfine component J, F_1, F = 1, 2, 3 → 0, 1, 2 (Caselli et al. 1995; Pagani et al. 2009).

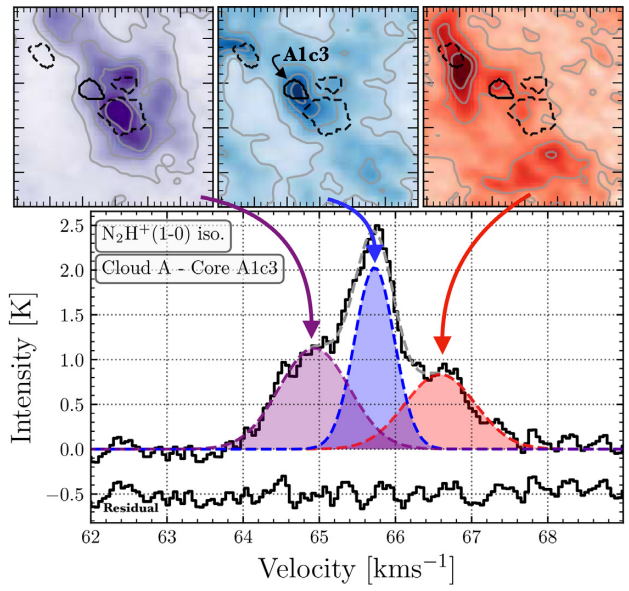

Figure 5. Gaussian decomposition of the velocity components towards core A1c3 (Section 3.3). The spectrum of the isolated hyperfine component of N_2H^+ (1−0) is shown as a black solid line, whilst the three velocity components identified by the SCOUSEPY routine are shown as the dashed and filled coloured lines. The total fitted spectrum is shown as a grey-dashed line, and the residual of observed spectrum minus the total fitted line is shown as a solid black line centred at −0.5 K. Shown in the above panels are maps towards Core A1c3 of the N_2H^+ (1−0) intensity integrated over the approximate velocity range covered by each component. These maps have been overlaid with grey contours also showing the N_2H^+ (1−0) intensity, in levels that have been chosen to best highlight the emission morphology. Shown as a solid black contour is the boundary of Core A1c3, and the black-dashed contours show the remaining cores within this region (also see Fig. 2). This Figure highlights that the brightest velocity component has the best spatial correspondence to the continuum peak.

on these maps are the cores, and the solid black contour corresponds to core A1c3; over which the spectrum shown in the main panel has been taken. These panels clearly show that, although several velocity components overlap at the region of core A1c3, only the brightest component (shown here in blue) has a spatial morphology that peaks at the position of the core A1c3. The purple and red components appear to peak more towards cores A1c1/2 and A1c4, respectively. This then validates the assumption that the brightest velocity component observed in N_2H^+ (1−0) is associated with the continuum core. We perform a similar manual check of the N_2H^+ (1−0) emission morphology towards each core and find that this assumption also holds in the vast majority of cases. For the 2−5 potential exceptions (i.e. ∼5 per cent of the overall sample), it is, however, not definitively clear if the choice of a lower brightness velocity component would be preferable. These will be investigated further in a future work in this series, in which we will conduct a more comprehensive pixel-by-pixel decomposition of the velocity structure within each cloud (Henshaw et al., in preparation).

We correct the observed velocity dispersion, $\sigma_{\rm obs}$, for the minor contribution of the velocity resolution:

$$\sigma_{\rm v}^2 = \sigma_{\rm obs}^2 - \frac{\Delta {\rm v}_{\rm res}^2}{8\ln 2}, \tag{4}$$

where ${\rm v}_{\rm res} \sim 0.1\,{\rm km\,s^{-1}}$ is the velocity resolution of the observations (see Section 2). Moreover, we determine the contribution of the non-thermal motions to the velocity dispersion. This can be calculated as (Fuller & Myers 1992; Henshaw et al. 2016a)

$$\sigma_{\rm NT}^2 = \sigma_{\rm v}^2 - \sigma_{\rm T}^2 = \sigma_{\rm v}^2 - k_{\rm B}T_{\rm kin}\left(\frac{1}{\bar{m}} - \frac{1}{m_{\rm obs}}\right), \tag{5}$$

where $\sigma_{\rm NT}$ and $\sigma_{\rm T}$, are the non-thermal, and the thermal velocity dispersions, respectively. $T_{\rm kin}$ is the kinetic temperature of the gas, which we assume $T_{\rm kin} = T_{\rm dust}$, $k_{\rm B}$ is the Boltzmann constant, $\bar{m}$, and $m_{\rm obs}$ refer to the mean molecular mass (2.37 a.m.u) and observed molecular mass (29 a.m.u for N_2H^+), respectively. We examine this non-thermal contribution with respect to the sound speed of the gas. This is referred to as the sonic Mach number,[7] or $\mathcal{M}_{\rm s} = \sigma_{\rm NT}/\sigma_{\rm T}$. We find $\mathcal{M}_{\rm s} = 1.7^{+0.9}_{-0.8}$ across the cloud sample (see Table A2). The uncertainty from the fitting procedure on $\sigma_{\rm obs}$ is typically ∼5 per cent, which is taken as the uncertainty on $\sigma_{\rm v}$. This ∼5 per cent uncertainty also applies to $\sigma_{\rm NT}$ and $\mathcal{M}_{\rm s}$ for the quiescent cores. For the star-forming sources, we propagate the higher temperature uncertainty, and determine a ∼30 per cent on $\sigma_{\rm NT}$, and ∼50 per cent on $\mathcal{M}_{\rm s}$.

The non-thermal motions could be indicative of turbulent motions within the cores, or the ordered global collapse of the cores (e.g. Kauffmann, Pillai & Zhang 2013). Fig. 3 shows histograms of $\mathcal{M}_{\rm s}$ for the whole sample, and for the star-forming cores and quiescent (non-star-forming) cores only. We find that the distribution for the star-forming cores peaks towards higher values of $\mathcal{M}_{\rm s}$ compared to the quiescent (non-star-forming) cores. Indeed, we determine median values of $\mathcal{M}_{\rm s} = 1.57$ for the quiescent cores, and $\mathcal{M}_{\rm s} = 2.04$ for star-forming cores. We conduct a Kolmogorov–Smirnov test to determine the significance of this difference. We find a p-value of 0.11 for the samples, which cannot reject the null hypothesis that the two samples are the same at a < 10 per cent accuracy. Thus, we cannot statistically confirm if the $\mathcal{M}_{\rm s}$ values from star-forming and quiescent cores are from the same distribution. None the less, it is worth highlighting that a difference in the sonic Mach number for star-forming and non-star-forming cores across a similar size scale has already been noted within the literature, and attributed to feedback effects from embedded young-stellar objects (e.g. Sánchez-Monge et al. 2013).

3.4 Stability assessment

In this section, we assess the stability of the cores against gravitational collapse. We consider that self-gravity is the only force causing the collapse of the cores (e.g. neglected any added pressure caused by the host cloud), and determine the balance against thermal support, thermal, and turbulence support, and then consider any necessary magnetic fields required for further support against collapse.

3.4.1 Thermal support

We, first, investigate the support from gravitational collapse by the thermal pressure only. To do so, we determine the so-called Jeans mass, $M_{\rm J}$, which gives the maximum mass that can be supported by thermal pressure, and the Jeans length $\lambda_{\rm J}$, which gives the length-scale of the fragmentation. The Jeans mass can be given as (Jeans 1902)

$$M_{\rm J} = \frac{\pi^{5/2}c_{\rm s}^3}{6G^{3/2}\rho^{1/2}}, \tag{6}$$

[7]Note that here we have determined the sonic Mach number ($\mathcal{M}_{\rm s} = \sigma_{\rm NT}/\sigma_{\rm T}$) using the 1D velocity dispersion ($\sigma_{\rm NT}$). However, this value can be converted to the 3D sonic Mach number by accounting for a factor of $3^{0.5}$; $\mathcal{M}_{\rm s,3D} = 3^{0.5}\mathcal{M}_{\rm s}$ (e.g. Palau et al. 2015).

where ρ is the volume density of the core, and the sound speed is $c_s = k_B T_{kin}/m_H\mu_{H_2} \sim 0.25\,km\,s^{-1}$ at the median core dust temperature of 18 K, and G is the gravitational constant. We find values of the Jeans mass across the core sample of $M_J = 0.8^{+0.3}_{-0.1}\,M_\odot$, and when using the background subtracted mass estimates: $M_J^b = 1.4^{+0.9}_{-0.5}\,M_\odot$. We compare these masses to the measured core masses, and find median ratios of $M/M_J = 19.9^{+45.7}_{-15.7}$ ($M^b/M_J^b = 2.7^{+19.4}_{-2.3}$). These ratios of $M/M_J > 1$ then show that the cores are potentially unstable to gravitational collapse if not additionally supported. These gravitationally unstable cores are potentially susceptible to further fragmentation. We estimate the corresponding Jeans length using

$$\lambda_J = c_s \left(\frac{\pi}{G\rho}\right)^{1/2}. \quad (7)$$

We find a value of the Jeans length across the sample of $\lambda_J = 0.03^{+0.01}_{-0.01}$ pc (or 6512^{+2439}_{-1756} au), and $\lambda_J^b = 0.06^{+0.03}_{-0.02}$ pc (or 12022^{+6783}_{-3804} au). Comparing these values to the projected radius of the cores we find a ratio of $R_{eff}/\lambda_J = 1.36^{+0.66}_{-0.54}$, highlighting that these Jeans unstable cores could then fragment on size scales similar to the current observed core size scales. We will discuss this again later in this work, when we investigate the hierarchical structure of these cores using higher resolution data sets.

3.4.2 Thermal and turbulence support

We now assess the balance of the total kinetic energy, E_{kin}, including both the thermal and turbulent pressure against the gravitational potential energy, E_{pot}. These energy terms can be equated to produce the commonly used virial parameter, α_{vir} (e.g. Bertoldi & McKee 1992). In the idealized case of a spherical core of uniform density supported by only kinetic energy (i.e. no magnetic fields), the virial parameter takes the form

$$\alpha_{vir} = a\frac{5\sigma_v^2 R_{eff}}{GM}, \quad (8)$$

where R_{eff} is the effective radius of the core, M is the total mass of the core, σ_v is the line-of-sight velocity dispersion, i.e. including both the thermal and turbulent broadening (α_{vir} does not account for any systematic infall/outflow motions; see e.g. Kauffmann et al. 2013). The factor a accounts for systems with non-homogeneous and non-spherical density distributions, and for a wide range of core shapes and density gradients takes a value of $a = 2 \pm 1$ (see Bertoldi & McKee 1992). In the above, a value of $\alpha_{vir} < 2$ indicates the core is sub-virial and may collapse, whereas for a value of $\alpha_{vir} > 2$ the core is supervirial and may expand.

We find virial parameters across the sample of $\alpha_{vir} = 0.7^{+0.5}_{-0.4}$ ($\alpha_{vir}^b = 2.3^{+3.8}_{-1.5}$). The propagated error on α_{vir} is ∼50 and ∼60 per cent for the quiescent and star-forming cores, respectively. We then find that the majority of cores within our sample have α_{vir} less than 2 and therefore would appear to be bound and unstable to collapse. That said, these virial parameters are closer to a pressure balance than when only considering thermal pressure, which highlights the relative importance of the non-thermal motions in support against gravitational collapse. It should also be noted that this result appears sensitive to the background subtraction.

We also assess the fragmentation of the cores using the total Jeans mass, $M_{J,tot}$, which accounts for both the contribution of the thermal and non-thermal velocity dispersion. This can be calculated by substituting the σ_v for c_s in equation 8 (e.g. Palau et al. 2015; Sadaghiani et al. 2020). We find values of $M_{J,tot} = 4.4^{+9.4}_{-3.2}\,M_\odot$ ($M_{J,tot}^b = 8.7^{+14.6}_{-6.4}\,M_\odot$), or as a ratio to the measured mass $M/M_{J,tot} = 3.1^{+9.4}_{-1.8}$ ($M/M_{J,tot}^b = 0.5^{+1.8}_{-0.4}$). These values of the total Jeans mass are typically factors of a few higher than when accounting for only the thermal support (see Section 3.4.1), and more comparable to the measured masses. However, as shown by the virial parameter, values of $M/M_{J,tot} > 1$ highlight that the cores are likely to collapse and/or fragment unless further supported.

The parameters determined in this section for each source are given in Table A2. We also note, we have investigated the virial state and total Jeans mass of the cores when using the N_2H^+ cubes that have been corrected for the zero-spacing, i.e. feathered with the single-dish observations. When doing so we still find that the majority of the cores are kinematically sub-virial and have masses larger than their associated Jeans masses, suggesting that they may be susceptible to collapse and fragmentation if other means of support, e.g. magnetic fields, are not significant.

3.4.3 Thermal, turbulence, and magnetic support

Lastly, we assess the relative importance of the magnetic field in support against gravitational collapse. To do so, we follow Henshaw et al. (2016b) and calculate the virial parameter that includes the magnetic field contribution (Pillai et al. 2011):

$$\alpha_{B,vir} = a\frac{5R_{eff}}{GM}\left(\sigma_v^2 - \frac{\sigma_A^2}{6}\right), \quad (9)$$

where the Alfvén velocity is $\sigma_A = B(\mu_0\rho)^{-1/2}$, in which B is the magnetic field strength and μ_0 is the permeability of free space. Here, then we ask: how much magnetic field pressure is required in addition to turbulence and thermal pressure to support the cores against gravity? To do so, we set $\alpha_{B,vir} = a = 2$, and solve equation (9) for B for all cases where $\alpha_{vir} < 2$ (Section 3.4.2). We find values of $\sigma_A = 0.91^{+0.49}_{-0.45}\,km\,s^{-1}$ ($\sigma_A^b = 0.65^{+0.36}_{-0.37}\,km\,s^{-1}$), which correspond to Alfvén Mach numbers of $\mathcal{M}_A = \sigma_A/\sigma_T = 3.76^{+2.08}_{-1.88}$ ($\mathcal{M}_A^b = 2.75^{+1.48}_{-1.55}$). The range of magnetic field strengths required for the stability of the $\alpha_{vir} < 2$ cores is then $B = 520^{+470}_{-242}\,\mu G$ (or $B^b = 271^{+300}_{-181}\,\mu G$).

We compare these measurements to the Crutcher et al. (2010) relation linking the magnetic field strength (determined from Zeeman splitting) and volume density:

$$B_{med} \approx \frac{1}{2}B_0\left(\frac{n(H)}{n_0}\right)^{2/3} \approx \frac{1}{2}B_0\left(\frac{2n_{H_2}}{n_0}\right)^{2/3}, \quad (10)$$

where $B_{med} = B_{max}/2$, and for $n(H) > n_0$ where $n_0 = 300\,cm^{-3}$, $n(H) = 2n_{H_2}$, and $B_0 = 10\,\mu G$. We find values of $B_{med} = 1206^{+572}_{-411}\,\mu G$ ($B_{med}^b = 543^{+343}_{-238}\,\mu G$), or $B/B_{med} = 0.49^{+0.26}_{-0.23}$ ($B^b/B_{med}^b = 0.39^{+0.17}_{-0.20}$). This shows that the magnetic field required for the additional support against gravitational collapse could then be more than achieved if these cores follow the Crutcher et al. (2010) relation, which is broadly consistent with the typical magnetic field strengths observed within molecular clouds (Pillai et al. 2015, 2016; Soam et al. 2019; Tang et al. 2019).

In a comparable resolution 3 mm dust continuum study of the cores within the north portion of cloud H, Henshaw et al. (2016a) found that values of $B \sim 590\,\mu G$ are required to stabilize the cores (or $B \sim 830\,\mu G$ when accounting for the $\alpha_{B,vir} = 2$ imposed in this work). This value is broadly consistent with the range given by the standard deviation around the median value for the core sample (287–1000 μG). In the southern portion of Cloud H studied in this work, we estimate a range of $B \sim 278-704\,\mu G$, suggesting that the magnetic field required for support across this whole filament is reasonably constant. Moreover, in their study of cores identified from N_2D^+ (3−2) emission, Tan et al. (2013) and Kong et al. (2017) also

Table 3. Observational properties of the literature sample (Section 4.1). Tabulated is the type of structure, reference, the telescope used to study the core samples, the clouds covered, and the wavelength and angular resolution of the observations (mean of major and minor axis of beam size). The abbreviated references are Rathborne et al. (2006, R06), Henshaw et al. (2016a, H16), Henshaw et al. (2017, H17), and Liu et al. (2018b, L18).

Structure	Ref.	Telescope	Sample	λ (mm)	θ (arcsec)
Clump	R06	IRAM-30m	All	1.3	11
Core	H16	IRAM-PdBI	H	3	3.75
Core-frag.	H17	ALMA	H(6)	1	1
Core-frag.	L18	ALMA	Not I/J	1.3	1
Core	This work	ALMA	All	3	2.9

estimated that ∼1 mG B-fields were required for support against collapse. It is worth noting, however, that these magnetic field strengths required for support against collapse are around an order of magnitude larger than the mean plane-of-the-sky magnetic field strength measured over parsec scales for Cloud H (∼50 μG; Liu et al. 2018a).

4 MULTISCALE ANALYSIS OF CLOUD STRUCTURE

4.1 Homogenized sample of literature cores

We aim to make a comparison between the properties of the cores determined in this section to those presented within the literature (e.g. Kauffmann et al. 2013; Peretto et al. 2013; Sánchez-Monge et al. 2013). Moreover, as the IRDC sample studied here has been the subject of several mm-band studies at varying angular resolutions (e.g. Rathborne et al. 2006; Liu et al. 2018b), we also aim to study how the cores fragment over several orders of magnitude in size-scale.

The 10 clouds studied in this work have also been observed, at least in part, by the following studies: Rathborne et al. (2006, henceforth R06), Henshaw et al. (2016a, henceforth H16), Henshaw et al. (2017, henceforth H17), and Liu et al. (2018b, henceforth L18). The frequencies, angular resolutions, and source samples of each of these observations are given in Table 3. To follow the fragmentation of the cores, we first standardize the parameters used to determine the physical properties of the literature sample. In doing so, we attempt to remove any systematic variations of the properties produced by the differing underlying assumptions imposed by each work. We create a single table containing the observed flux densities and effective angular radii (i.e. $R_{\rm eff} = \sqrt{A/\pi}$) from each of the literature samples (see Table A3). We then recalculate the physical radius of each core assuming the cloud distances given in Table 1, and masses using equation (1) and the assumptions given in Section 3.2. We recalculate κ_ν for each set of observations using the frequencies given in Table 3, and $\beta = 1.75$ (Battersby et al. 2011) and $\kappa_0 = 0.9\,{\rm cm^2\,g^{-1}}$ (Ossenkopf & Henning 1994). We assume a constant dust temperature for all literature calculations of $T_{\rm dust} = 18\,{\rm K}$, which approximately corresponds to the mean dust temperature measured across the cores identified in this work (see Section 3.2). The standardized properties for the literature cores are provided in Table A3.

It should be noted, the homogenization of the literature data set neglects variations in physical properties, such as dust-opacity, gas-to-dust ratio, and temperature, which could vary as a function of the size-scale. However, these properties have not been accurately measured for the IRDC sample across all scales. Hence, the homogenized comparison presented here is favoured for its simplicity over, e.g. arbitrarily varying the temperature or opacity as a function of size. Assuming dust temperatures of $T_{\rm dust} = 10$ and 30 K rather than 18 K would cause the mass of a core identified at 3 mm to vary by factors of 2.0 and 0.57, respectively (see Section 3.2 for discussion of uncertainties on the temperature estimates of the star-forming sources). Additionally, assuming β values of 1.5 and 2, rather than 1.75, would cause the mass of a core identified at 3 mm to vary by factors of 0.79 and 1.25, respectively.

We define a referencing nomenclature for the structures within this catalogue based on the approximate scales over which the literature observations cover. For simplicity, we refer to the largest (0.1–1 pc) structures from R06 as clumps, the intermediate size (0.01–0.1 pc) structures identified in this work and H16 as cores, and the smallest structures identified by L18 and H17 as core fragments. It should, however, be kept in mind that this is a simplification for referencing purposes, and is solely based on their approximate size scales with no bearing on their stellar population formation potential (e.g. Williams, Blitz & McKee 2000). Moreover, due to varying distances and physical properties across the cloud sample, there is some cross-over between these groups, e.g. for the closest clouds, several R06 clumps have radii <0.1 pc, and therefore could be classified as cores based on their size-scales.

4.2 Mass– and linewidth–size relations

A simple first analysis using our extensive core catalogue is to plot the masses, velocity dispersion, and virial states as a function of size (e.g. Larson 1981).

4.2.1 Mass–size relation

Fig. 6 presents the mass as a function of the effective radius for the core sample identified within this work compared to sources taken from the literature. Shown as the black-outlined red points are the masses (M) and as the red points are the background-subtracted masses ($M^{\rm b}$) determined in Section 3.2 (see Table A2). Shown as the coloured points are the masses and effective radii from the homogenized literature core catalogue (Section 4.1). For a representative comparison, we also plot in Fig. 7 the core samples from Kauffmann et al. (2013, K13), Peretto et al. (2013, P13), and Sánchez-Monge et al. (2013, SM13).

Fig. 6 shows that smaller cores are typically less massive, within an order-of-magnitude scatter in mass for any given effective radius. Shown as the diagonal grey-dotted lines are constant mean number densities. We see that the core fragments have $n_{\rm H_2} \sim 10^{6-7}\,{\rm cm^{-3}}$, whereas the clumps have $n_{\rm H_2} \sim 10^{4-5}\,{\rm cm^{-3}}$. Showing that the smallest cores are less massive, yet significantly denser than their more massive counterparts. The larger clumps could, however, also achieve larger volume densities at the same size scales of the smaller cores and core fragments, in the likely case that they are centrally concentrated. This could imply that the derived volume density of the larger clump is smaller because most of their volume is at lower densities.

Overlaid in Fig. 6 are several commonly adopted thresholds for massive star formation, which we can compare to the observed cores. The horizontal black-dashed line, and the dark-shaded region is the limit above which a star can be considered high mass (∼8 $M_\odot$). Note that this mass limit does not account for a star formation efficiency,

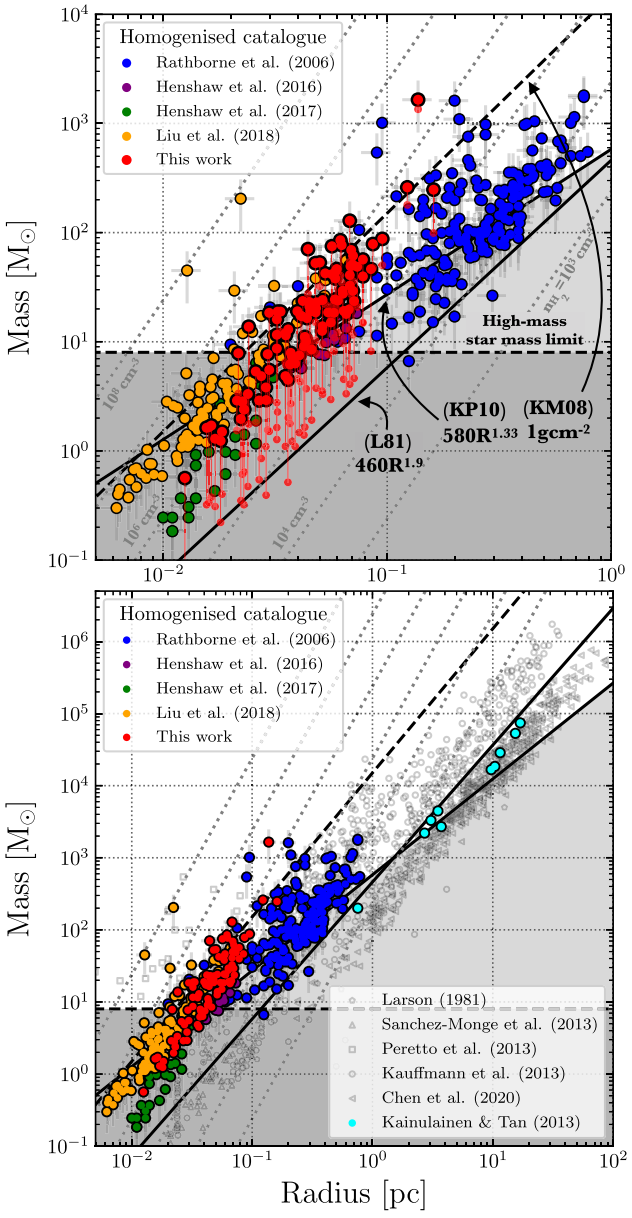

Figure 6. A comparison of the mass and sizes for the cores determined in this work, to samples taken from the literature, and mass–size relations and thresholds for massive star formation. Shown as the black-outlined red points are the cores studied in this work (M), which are connected to their corresponding lower background-subtracted masses ($M^{\rm b}$; see Table A2). Highlighted as the coloured points are the mass and the sizes of the cores and/or clumps determined by Liu et al. (2018b), Henshaw et al. (2016a), Henshaw et al. (2017), and Rathborne et al. (2006), which have cross-over with the IRDC sample examined in this work. The properties of these cores have been recalculated using the same assumptions outlined in this work (Section 4.1). (lower panel) Shown as the grey open points are the properties taken directly from Larson (1981), Kauffmann et al. (2013), Peretto et al. (2013), Sánchez-Monge et al. (2013), and Chen et al. (2020). Overlaid as the diagonal solid black lines are the mass–radius relations taken from Larson (1981, L81), and high mass star formation thresholds taken from Krumholz & McKee (2008, KM08) and Kauffmann & Pillai (2010, KP10). The KP10 relation has been scaled by a factor of 1.5 to match the dust opacity used throughout this paper. The horizontal dotted black line shows the mass threshold of high-mass stars (>8 $M_\odot$). The dashed diagonal grey lines show constant number densities (as labelled).

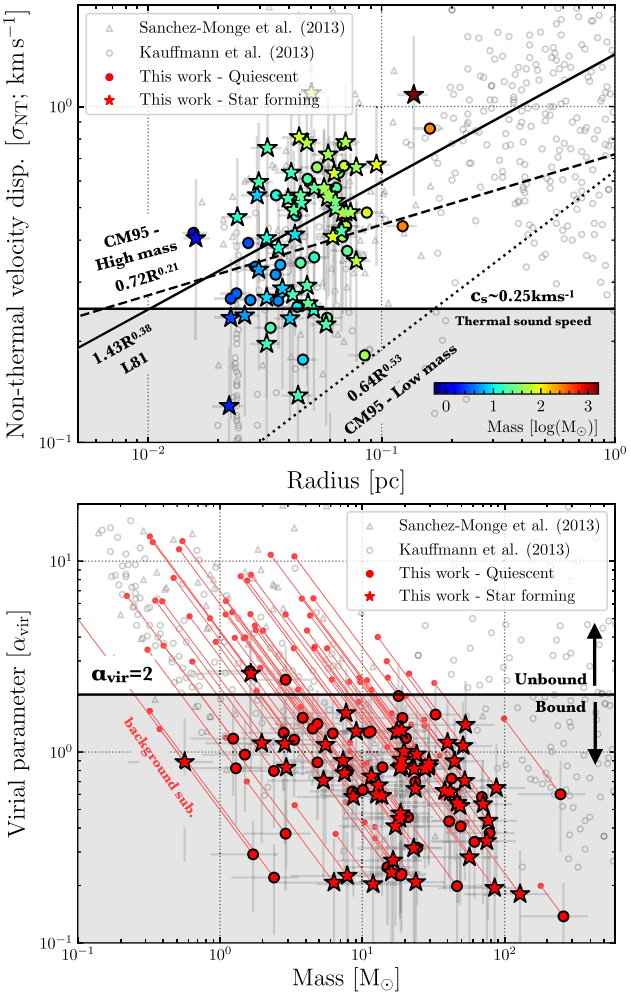

Figure 7. Dynamical state of the identified cores. The upper panel shows the non-thermal velocity dispersion as a function of the effective radius, and the lower panel shows the virial parameter as a function of the mass. Shown as the black-outlined circle and the star markers are the cores studied in this work that have been identified as quiescent and star forming, respectively (see Section 3.1). The points in the upper panel have been coloured according to their measured masses, as shown by the inset log-scale colour bar. In the lower panel, also shown by the red points without an outline are the corresponding background-subtracted properties (see Table A2). Shown as the grey open circles in both panels is the core samples from Kauffmann et al. (2013, K13) and Sánchez-Monge et al. (2013). The diagonal and horizontal black lines shown in the upper panel represent the Larson (1981, L81), Caselli & Myers (1995, CM95) low- and high-mass linewidth–size relations, and the thermal sound speed of the gas ($c_{\rm s} = (k_{\rm B}T_{\rm kin})/(m_{\rm H}\mu_{\rm p}) \approx 0.25\,{\rm km\,s^{-1}}$ for $\mu_{\rm p} = 2.37$ and $T_{\rm kin} = 18$ K). The horizontal black line shown in the lower panel represents the limit between ($\alpha_{\rm vir} < 2$) a bound core, and ($\alpha_{\rm vir} > 2$) unbound core with non-homogeneous and non-spherical density distribution (K13).

and therefore represents a lower limit for the required mass within a structure. Ultimately, any core with a mass lower than this threshold cannot in its current state form a high-mass star. Also overlaid in Fig. 6 as several black diagonal lines are often quoted mass–size relations.

The first of these mass–size relations is from Larson (1981, henceforth L81), and is given as $M = 460R^{1.9}$, where the normalization approximately relates to the mass surface density of their sample of local sources ($\Sigma = 460/\pi$ $M_\odot$ pc^{-2}), and M and R are the mass and the

radius in units of $M_\odot$ and parsec.[8] We see that almost all of the clumps and cores within the homogenized core catalogue (all coloured data points) sit above the L81 relation. The reason for this difference, which can be up to an order of magnitude for the smallest cores, could be a result of several factors. First, there are several systematics to consider. L81 defined the size as the is maximum linear extent of the structure (i.e. larger than $r_{\rm eff}$ used here). Secondly, the L81 mass estimates are determined from fundamentally different observations than used in this work. In this work, we analyse the dust continuum emission to estimate the masses, yet L81 used molecular line (e.g. CO) excitation arguments and simple assumptions about the geometry (see e.g. Lada & Dame 2020 for further discussion of how different mass tracers can cause scatter in the mass–size relation). Thirdly, the ALMA continuum observations presented within this work suffer from spatial filtering, which may affect this comparison to sizes and masses determined primarily from single-dish observations.

With the above systematics in mind, it is then worth considering that there may be an alternative interpretation of this result. On the largest scale (>1 pc), we see that the clouds are in broad agreement with the L81 relation (see lower panel of Fig. 6). The increase in M relative to L81 seen at smaller $r_{\rm eff}$ (<0.1 pc) could then be explained by the fragmented structure of the clouds, and, on the smallest scales, the density profiles of the cores themselves (see e.g. Kauffmann et al. 2010a,b; Ballesteros-Paredes, D'Alessio & Hartmann 2012 for discussion). The L81 relation fails to account for much of this complex structure we now know exists within molecular clouds (see e.g. McKee & Ostriker 2007 for references showing significant scatter in mass–size relations), and seen in our observations (see Fig. 2). It is then not all too surprising that we find this deviation, particularly as here investigate scales below that probed by L81.

Also overplotted in Fig. 6 are the HMSF relations proposed by Krumholz & McKee (2008, henceforth KM08) and Kauffmann & Pillai (2010, henceforth KP10). When determining their relation, KP10 reduced the Ossenkopf & Henning (1994) dust opacity used for the mass determination by a factor of 1.5 (see Kauffmann et al. 2010a). Following Dunham et al. (2011), we determine the relation to account for the dust opacity used throughout this work (see Section 3.2). The KP10 scale relation is hence given as $M = 580\,R^{1.33}$, where the M and R are the mass and the radius in units of $M_\odot$ and parsec. It is worth just briefly noting here again that the comparison to any empirical mass–size threshold may be complicated by systematics, such as the filtering characteristics that differ between observations (e.g. missing extended flux) and mass determination methodologies. For example, here KP10 used a dendrogram analysis, and based the relation on the non-background-subtracted mass estimates, yet we know that mass estimates can still vary depending on the contribution from fore/background emission. Hence, we emphasize caution when drawing any firm conclusion for the high-mass star-forming potential purely from such empirical mass–size thresholds (also see discussion in Section 4.3.1).

The analytically determined mass surface density threshold from KM08 is given as $\Sigma \sim 1\,{\rm g\,cm^{-2}}$, which is based on a model where fragmentation of massive cores is inhibited by radiative heating from surrounding lower mass protostars. The value of the mass surface density is required such that the lower mass protostars have high mass accretion rates, and hence are luminous enough to sufficiently heat the massive core. The KM08 threshold approximately corresponds to $M = 15000\,R^2$, in units of $M_\odot$ and parsec.

We find that the core sample sits around these two threshold relations, with the clumps scattering around the KP10 relation. The light grey-shaded region in Fig. 6 represents the parameter space below the $\sim$8 $M_\odot$ threshold for HMSF. We find that a several of cores within the size-scale of $\sim$0.05 pc sit above this shaded region, and hence would appear to be able to form a high-mass star when assuming no mass-loss or further fragmentation. We return the investigation of these sources as potential high-mass star-forming regions later in Section 4.3.2.

4.2.2 *Linewidth–size relation*

We now investigate how the dynamical state of the core sample depends on size scale and mass. In Fig. 7, we plot the non-thermal velocity dispersion (upper panel) as a function of effective radius. Here, we only show the cores determined in this work (the red points), as there is only a partial determination of the velocity dispersion for the homogenized literature sample. Moreover, where such measurements have been made for the homogenized literature sample, such a comparison is complicated by the use of different molecular lines, which may originate from fundamentally different gas properties and hence different regions within the cores. Bearing this in mind, in Fig. 7 we also show the core samples from SM13 and K13 (see their discussion of various molecular line probes used to compile this sample). We find that the cores identified in this work are in reasonable agreement within the scatter of those from the literature. Also overlaid as a diagonal solid black line in Fig. 7 is the L81 linewidth–size relation, which is given as $\sigma_{\rm v} = 1.1\,L^{0.38} = 1.1\,(2R)^{0.38} = 1.43\,R^{0.38}$, where L is the core diameter, and $\sigma_{\rm v}$ and R are in units of ${\rm km\,s^{-1}}$ and parsec. Note that the L81 relates to the total velocity dispersion, as opposed to the non-thermal velocity dispersion plotted in Fig. 7. We expect that this may cause a minor systematic, as the contribution of the thermal velocity dispersion is only small for the majority of cores (see Section 3.3). Moreover, we show the linewidth–size relations determined for both low and high mass within Orion by Caselli & Myers (1995, CM95). These are given by $\sigma_{\rm NT} = 0.64\,R^{0.53}$ for low mass, and $\sigma_{\rm NT} = 0.72\,R^{0.21}$ for high-mass cores, again in units of ${\rm km\,s^{-1}}$ and parsec (note the conversion to velocity dispersion from the linewidth provided in CM15). We find that the cores have range across all of the plotted linewidth–size relations, yet mostly cluster around the L81 and CM15 high-mass relations. We have highlighted in the upper panel of Fig. 7 the cores that are quiescent and star forming, and colour the points by their measured masses. We find no preference to any of the linewidth–size relations with the core masses or state of star formation. We find several cores have very narrow velocity dispersions, and sit significantly below the L81 relation, close to the CM15 low-mass relation. Shown as the grey-shaded region in Fig. 7 is $\sigma_{\rm NT} < c_{\rm s}$, or the regime where dynamical motions within the core are sub-thermal. Several cores from the K13 are also seen within this regime.

The lower panel of Fig. 7 shows the virial parameter as a function of mass for the cores identified in this work. Shown as the red circles and the red circles outlined in black are the masses and the virial parameters determined with and without background subtraction, respectively. Highlighted as a black horizontal line is $\alpha_{\rm vir} = 2$, which represents the boundary between gravitational bound and unbound cores (for a given core structure). We find that the majority of cores identified within this work have $\alpha_{\rm vir} \ll 2$, and therefore are expected

[8]Determined by equating $\sigma_{\rm v} = 1.1\,(L)^{0.38} = 1.1\,(2R)^{0.38}$ and $\sigma_{\rm v} = 0.42\,(M)^{0.2}$, where L is the core diameter, and solving for M and R (Larson 1981).

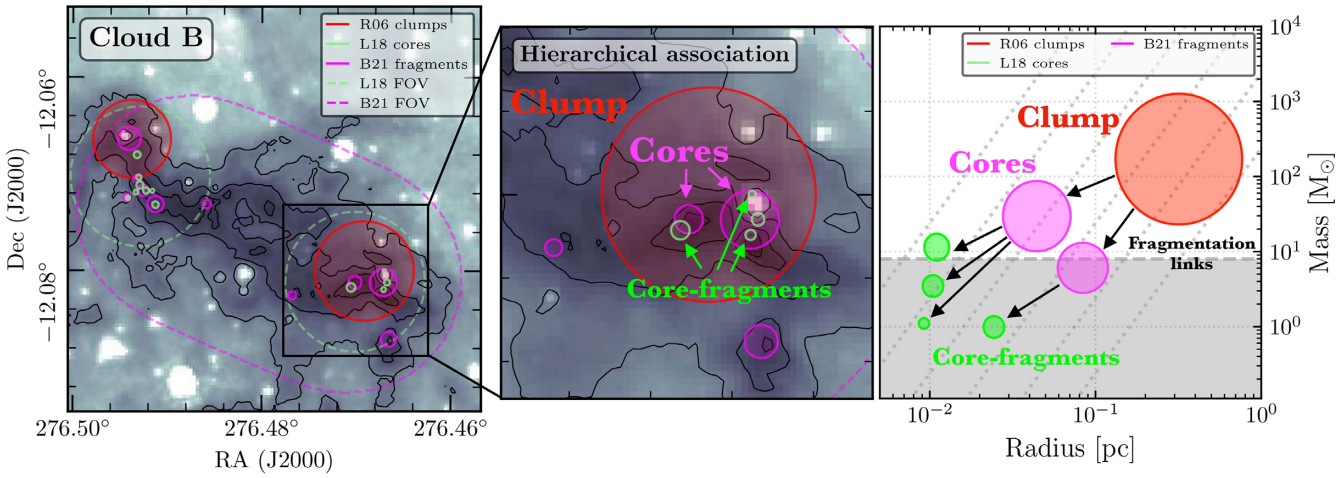

Figure 8. A schematic diagram showing the fragmentation linking procedure, which we use to determine a hierarchy of structures similar to a dendrogram across multiple data sets covering our cloud sample (Section 4.3). The left-hand panel shows the near- and mid-infrared extinction derived mass surface density map for Cloud B in grey scale, overlaid with the circles representing the position and sizes of the cores contained within the homogenized catalogue (Section 4.1). The red circles show the Rathborne et al. (2006, R06) clumps, the solid magenta circles show the cores identified in this work (B21), and the solid green circles show the core fragments identified by Liu et al. (2018b, L18). The dashed magenta and green lines show the field of view (FOV) of the ALMA observations presented in this work and in L18, respectively. The centre panel shows a zoom-in of the MM2 R06 core within Cloud B, which is highlighted on the left-hand panel by a solid black box. Here, the clump, core, and core fragment structures have been labelled. The right-hand panel shows the mass as a function of radius for the example MM2 region. Here, we show the fragmentation links between the host clump, and the cores and core fragments contained within its boundary.

to collapse without additional support. We find that when accounting for the background subtraction, many cores do move into the unbound regime ($\alpha_{\rm vir} > 2$). We find no clear trend between the virial parameters and the mass or star-forming state of the cores.

4.3 Fragmentation

4.3.1 Determination of hierarchical structure

In this section, we aim to follow and connect the mass distribution through fragmentation of the complete homogenized clump-core-core fragment sample. In effect, what we create in this analysis is a hierarchy of structures similar to a dendrogram, yet we recover many magnitudes in spatial scale by combining various sets of observations towards the same sources taken at differing spatial resolutions. To create this structure for each of the IRDCs studied here, we first order the data sets in the homogenized structure catalogue by decreasing angular resolution (see Table 3). We then take the largest scale clumps and the intermediate scale cores for a given IRDC (e.g. R06 and this work), and determine if the positions of the cores are contained within the boundaries of the clumps. This step is then repeated decreasing in scale, e.g. with the cores from this work and core fragments from L18. The result of this procedure is a structure catalogue with links between clumps that contain cores, and the cores that contain core fragments. Fig. 8 shows a schematic diagram of this fragmentation procedure within the MM2 clump within Cloud B, and how the determined fragmentation links can be interpreted through the mass–radius parameter space.

We highlight that the fragmentation analysis shown in Fig. 8 includes three clumps associated within mm-bright star-forming regions (Cloud C MM14, Cloud I MM3, and Cloud F MM9). These sources are particularly bright and add confusion to the core identification in the lower resolution observations from R06 such as, e.g. close-by lower brightness cores merge with the bright source. Moreover, these embedded sources can produce a large increase in temperature, and so our masses may be overestimated. The resultant large uncertainty on the mass estimate can, for example, cause R06 clumps to have masses that appear smaller than the contained cores. These have been highlighted in Fig. A1, and their hierarchical structure should be taken with caution.

Fig. 9 shows the mass as a function of radius for all the homogenized catalogue. Here, the circles, the crosses, and the plus sign markers represent the clumps identified by R06, the cores from this work, and the core fragments from L18, respectively. We highlight the size-scales that correspond to the cores (<0.1 pc) and core fragments (<0.01 pc) that are expected to form single stars, and the 0.1–1 pc scale clumps that fragment into multiple cores that are expected to form several stars (e.g. Williams et al. 2000). These lines show the connections according to their fragmentation (see appendix for all clouds plotted separately). We find that all the cores identified within this work originate from the larger scale cores identified by R06. Moreover, in many cases, several cores originate from the same parent R06 clump. We find that on smaller scales the cores identified here also fragment further, and in several cases also into multiple core fragments. This further highlights the hierarchical nature of the ISM, where structures can fragment at increasingly smaller scales.

Following the individual hierarchies in Fig. 9, we see that the connected structures can cross the KM08 and KP10 HMSF thresholds at different scales. At large scales (∼0.5 pc), we see that clumps can have a moderate number density (10^{4-5} cm^{-3}), and sit around the KP10 relation. At intermediate scales (0.1–0.5 pc), the cores have a higher density (10^{5-6} cm^{-3}), and are comparable to both the KM08 and KP10 relations. At the smallest scale (∼0.01 pc), the core fragments lie either below the mass (<8 M$_\odot$) threshold, or again under both the massive star formation relations. This then highlights the difficultly of these thresholds in predicting the high-mass star-forming potential of a region across any given spatial scale.

4.3.2 Identification of potential high-mass star-forming cores

In this section, we attempt to use the hierarchy within each cloud to identify the cores that present the best candidates for the early stages of HMSF. To do so, first, we impose that both the mass and

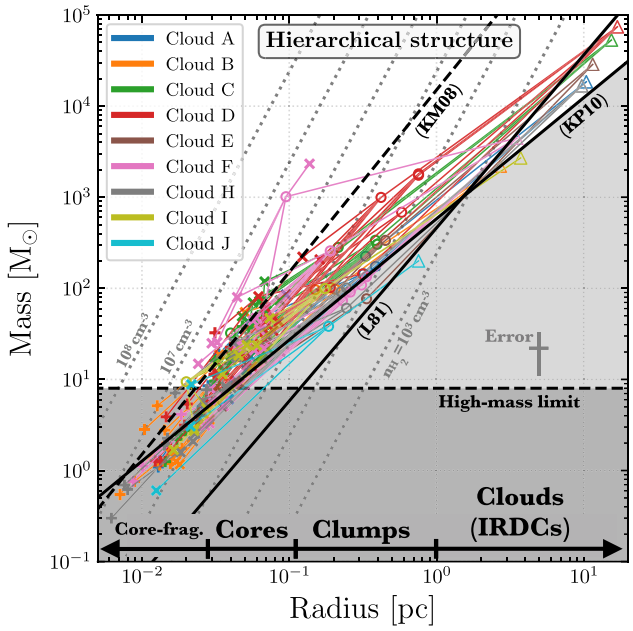

Figure 9. The clump-to-core fragment masses within each cloud as a function of the size-scale. The circles, the crosses, and the plus sign markers represent the clumps from R06, cores from this work, and the clumps from L18. The straight lines connect the symbols for each core/core fragment to the larger, host clump/core, and then cloud (see Fig. A1 in the appendix for all clouds plotted separately). The lines and the symbols have been coloured by cloud as indicated in the legend located in the upper left. The dotted diagonal grey lines show constant number densities (as labelled), and the black lines show the high mass star formation thresholds shown in Fig. 6. In the lower right, we show a representative uncertainty range between ∼15 and ∼50 per cent on the radius and mass, respectively.

the background-subtracted mass of the cores identified in this work, M_c and M_c^b, must be $>16\,M_\odot$, hence separating those cores that have enough mass to form at least a high-mass star when assuming a star formation efficiency of ∼50 per cent (see e.g. Tanaka, Tan & Zhang 2017; Liu et al. 2020a). Secondly, we restrict the sample by the number of core fragments, n_{cf}, contained within each core. Cores with $n_{cf} = 0$ are included, as these represent the lowest level of the hierarchy, i.e. those that are high mass, yet do not appear to fragment. Cores with $n_{cf} = 1$ are also included, as the core fragment corresponds to a central emission peak, and hence these also represent cores that do not fragment. Cores with $n_{cf} > 1$ are included only if at least one of the core fragments has a mass of $M_{cf} > 16\,M_\odot$. We stress once more that the cores could have a complex 3D, density, and temperature structures that could influence this analysis. For example, the emission peak(s) could correspond to a central density peak, or, in the case of a star-forming sources, an increase in temperature (e.g. those with a 70 μm point source; see Section 3.2). A more in-depth study of the kinematic and chemical composition of these cores will be used to address this in the future, and here we make the simple, general assumption that the identified hierarchical structure is due to the physical fragmentation. We separate this high-mass core sample by those with and without signs of ongoing star formation (i.e. have no associated infrared point source emission; see Section 3.2).

Of the sample of 96 cores used for this analysis, we find that 19 cores satisfy the above requirements as potential candidates for HMSF. Out of these, we find that 6 show no signs of active star formation, whilst 13 have signs of active star formation.[9] Fig. 10 shows the mass and radius of the high-mass cores with the connection to their host clumps and contained core fragments. We plot separately the cores that have been classified as quiescent and star forming in the upper and lower panels, respectively. For reference, we also show the cores identified in this analysis that do not meet the background-subtracted mass threshold of ($M_c^b > 16\,M_\odot$).

We first focus on the six quiescent high-mass cores. We see that these are distributed across clouds A, C, and D, which contain 1, 2, and 3 core(s), respectively. The positions of these quiescent cores are shown in Fig. 2 with cyan contours. We find that these have radii ranging from 0.05 to 0.12 pc, and masses from 42 to 260 $M_\odot$ (background-subtracted masses of 21–180), which correspond to mean mass surface densities of 0.7–1.1 g cm^{-2}. We have determined the dynamical properties of these cores. We find sonic Mach numbers across this sub-sample from 1.9 to 2.9 (median 2.0), and virial parameters from 0.14 to 0.73 (median 0.39). This then highlights that these cores contain trans-sonic non-thermal motions, are predominately kinematically sub-virial and require moderate magnetic field strengths of 780–1380 μG (median 976 μG) for support against collapse. Without magnetic support, these cores would then be expected to form high-mass stars on the scale of a free-fall time, which we calculate ranges between 30 000 and 50 000 yr for the sample.

The 13 high-mass cores that show signs of on-going star formation have radii ranging from 0.04 to 0.10 pc, and masses in the range of 24–129 $M_\odot$ that correspond to mass surface densities of 0.6–2.4 g cm^{-2}. It should be kept in mind that the presence of star formation within these cores most likely means that the assumed dust temperature measurement is too low, and because of this these mass estimate have a larger associated uncertainty of ∼30 per cent (Section 3.2). We find Mach numbers for these sources of 1.7–4.5 (median 2.4), virial parameters from 0.18 to 1.39 (median 0.54), which would require magnetic field strengths of 592–2570 μG (median 934 μG) for additional support. The properties of this sub-sample are then generally higher than the quiescent high-mass core sample.

We now assess how the properties of the high-mass cores compare to the modes of HMSF introduced in Section 1. The turbulent core accretion theory makes predictions for the sizes of massive pre-stellar cores (and thus early-stage cores) in IRDC environments. McKee & Tan (2003, their equation 20) propose that the radius of the core (R_c) is linked to the core mass (M_c) and the mean mass surface density of the cloud (Σ_{cl}): $R_c = 0.057(R_c/60M_\odot)^{1/2}\Sigma_{cl}^{-1/2}$ pc. This then predicts that for a typical mass surface density across the cloud sample of Σ_{cl} ∼0.1 g cm^{-2} (Kainulainen & Tan 2013), a 16 $M_\odot$ core would have a radius of ∼0.09 pc, respectively. Using the upper limit of the mass surface density within the clumps instead of the average across the cloud, we predict a 16 $M_\odot$ core would have a radius of 0.04 pc. These values are broadly comparable to the measured size range of high-mass core sample therefore the existence of these structures is consistent with above predictions from the core accretion theory.

Several mechanisms have been proposed to support high-mass cores against significant fragmentation in core accretion theory. The aforementioned Krumholz & McKee (2008) relation predicts that the suppression of fragmentation is a result of the warming from a population of lower mass protostars. This requires the environments surrounding the young high-mass stars to have high mass surface

[9]The quiescent high-mass cores are A3c3, C2c1, C1c1, D8c1, D6c5, and D6c4. The high-mass star-forming cores are A1c1/2, B2c10, C2c2, C2c3/5, C2c6, D5c7, C6c1/2, D9c1/2, F4c5, F4c8, F4c10, H3c3, and I1c1.

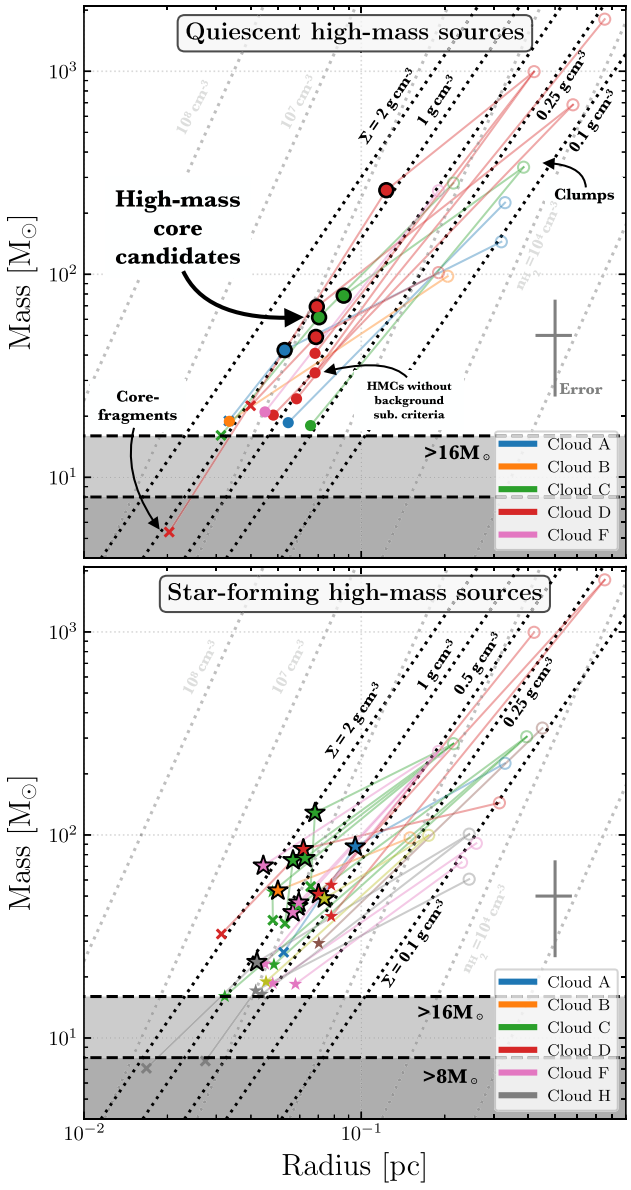

Figure 10. The 19 high-mass quiescent and star-forming core candidates (HMCs; see Section 4.3.2). As in Fig. 9, we show the mass fragments within each cloud as a function of the size-scale. We highlight with the black-outlined symbols the cores identified within this work, which have been singled out as high mass ($M_c > 16\,M_\odot$ and $M_c^b > 16\,M_\odot$) without further fragmentation. We plot separately the cores that have been classified as quiescent and star forming in the upper and lower panels, respectively. We also show as the filled symbols with no outline cores identified in this paper that do not meet the background-subtracted mass threshold ($M_c^b > 16\,M_\odot$). The Rathborne et al. (2006) clumps and Liu et al. (2018b) core fragment shown as the faded open circles and the crosses, respectively. The dotted diagonal faded grey lines show constant number densities (as labelled), and the black-dotted diagonal lines show constant mass surface density (Σ; as labelled). In the lower right, we show a representative uncertainty range between ∼15 and ∼50 per cent on the radius and mass, respectively.

densities ($\Sigma \sim 1\,g\,cm^{-2}$), such that the protostars have high accretion rates. It is then interesting to consider that the cores that show signs of active star formation typically (6 of 13) have mass surface densities of $>1\,g\,cm^{-2}$. An alternative mechanism for the suppression of fragmentation is from strong magnetic field strengths, which we estimate should be of the ∼1 mG to support against gravitational collapse. Magnetic field strengths similar of this order have been previously observed within molecular clouds (Pillai et al. 2015, 2016; Soam et al. 2019; Tang et al. 2019; Liu et al. 2020b).

It should be noted that there are high-mass cores that have been identified in this work that do fragment on smaller scales. We find that three cores meet the above mass requirements, yet fragment into more than two lower mass core fragments.[10] These would be interesting candidates to follow-up in the context of lower mass star formation, or future high-mass cores.

Lastly, we highlight several future observations that would help assess the high-mass star-forming potential of these cores. First, cores C1c1 (quiescent) and I1c1 (star forming) were not covered by the Liu et al. (2018b) observations, and therefore it would be interesting to investigate if these fragment in high spatial resolution observations. Secondly, it would be interesting to investigate if any of these sources contain signs of lower mass star formation that would be evident within the infrared emission, such as searching for outflows. A comparison to the positions outflows in Cloud C shows that the high-mass (quiescent) core C1c1 could indeed already contain embedded lower mass protostars (Feng et al. 2016a,b; Kong et al. 2019). Third, the quiescent high-mass core C2c1 has been observed at high resolution by both Zhang et al. (2015) and Kong et al. (2017). These studies find that this core contains $\sim 30\,M_\odot$ on the scale of $\sim 10^{-3}$ pc, has no shock or outflow tracer emission and has significant N_2D^+ (3–2) emission. Indicating that core C2c1 is chemically young, and a particularly interesting target for follow-up studies of the earliest stages of HMSF. Lastly, measurements of the magnetic field strength across the cores would be useful in assessing their stability.

4.3.3 From clouds (∼1 pc scales) to cores (∼0.1 pc scales)

We now use this hierarchical structure to investigate how the global properties inherited from the IRDC (∼1 pc scales) affect the properties of their ∼0.1 pc scale cores identified here, and how the properties of these ∼0.1 pc scale cores then influence the smallest ∼0.01 pc scale core fragments into which they fragment.

We first compare the cloud properties to the properties of the cores identified within this work (Table A2). The cloud properties are given in Table 1, which have been taken from Kainulainen & Tan (2013, their table 1). These authors determine the masses of the clouds from the combined mid- and near-infrared extinction maps (see Fig. 2), and the velocity dispersion from ^{13}CO emission cubes (Jackson et al. 2006). Also included in Table 1 are the mean *Herschel* derived dust temperatures measured within the footprint of the ALMA observations for each cloud, which are used to determine the corresponding non-thermal velocity dispersions and sonic Mach numbers (following Section 3.2).

Fig. 11 presents the comparison between the core and cloud properties.[11] In columns of panels from left to right, we show the number, mass, effective radius, minimum separation, non-thermal velocity dispersion, and virial parameter for the identified cores on

[10] Cores B1c1/2/3, D5c5/6, F1c1.

[11] It is worth noting that Cloud G is not included within this analysis, as no continuum cores were identified within the mapped region of this source (Section 3). Moreover, following Kainulainen & Tan (2013), Cloud E has been removed from this analysis due to its complex velocity structure observed in the ^{13}CO observations, and hence the large uncertainty associated with the cloud dynamical properties.

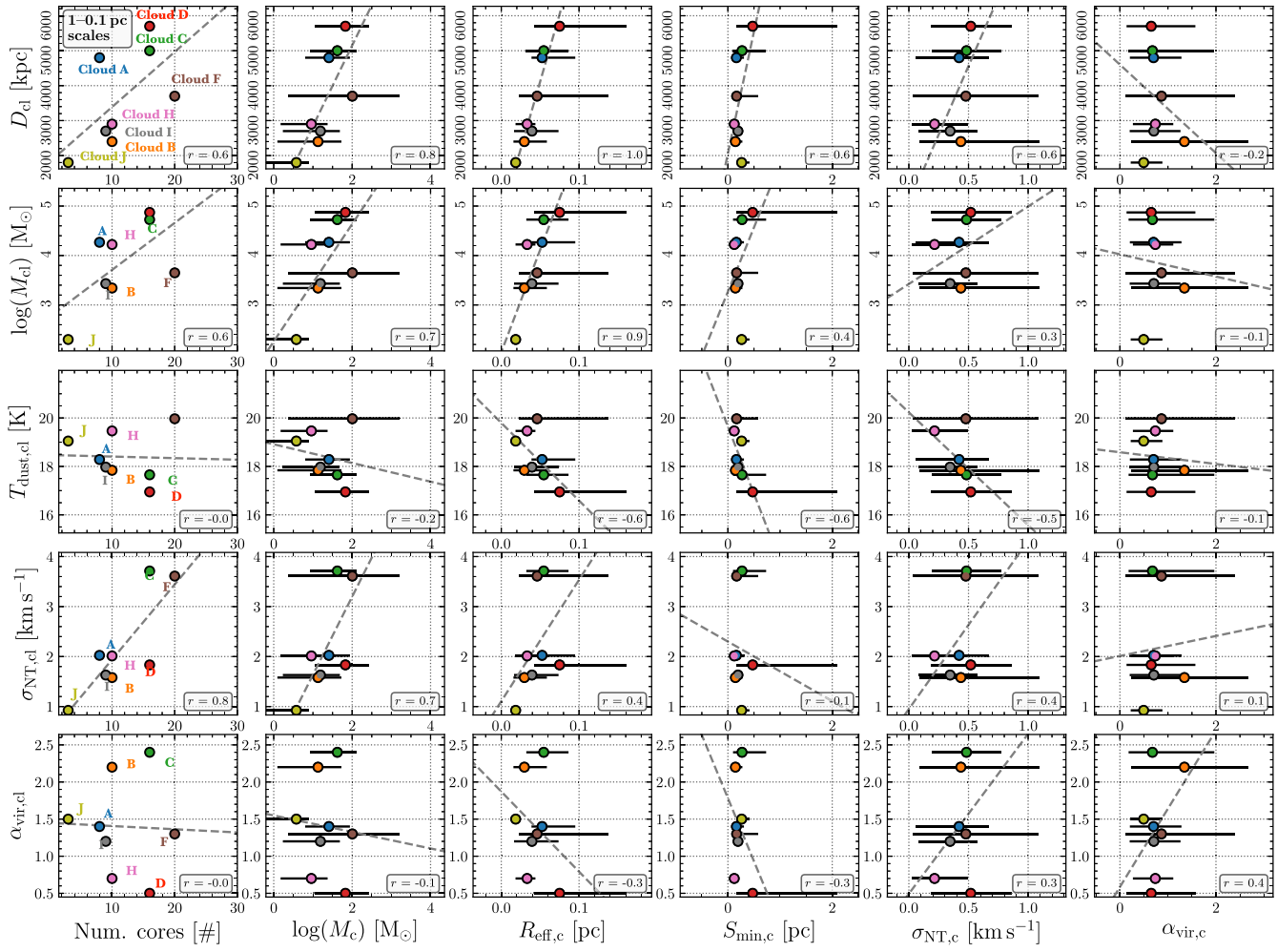

Figure 11. A comparison between the properties of the ($\sim$ 0.1 pc scale) cores identified in this work, and their host ($\sim$ 1 pc scale) cloud properties (see Table 1). In columns from left to right, we show the number, logarithm of the mass (M_c), effective radius ($R_{eff,c}$), minimum separation ($S_{min,c}$), non-thermal velocity dispersion ($\sigma_{NT,c}$), and virial parameter ($\alpha_{vir,c}$) of the cores within each cloud on the x-axis. In rows from top to bottom, we show the cloud distance (D_{cl}), logarithm of the mass (M_{cl}), mean dust temperature ($T_{dust,cl}$), non-thermal velocity dispersion ($\sigma_{NT,cl}$), and virial parameter ($\alpha_{vir,cl}$) on the y-axis. The points shown in all except the first column represent the mean core properties, and the error bars show the range between the minimum and maximum values of the cores within a given cloud. As highlighted in the upper left-hand panel, the colour of each point corresponds to their host cloud. The dashed grey lines show the linear relation ($y = ax + b$) from the least-squares fit of the variables plotted on the x- and y-axis. The Pearson's-r value are given within the upper right of each panel.

the x-axis. In rows of panels from top to bottom, we show how the core properties vary with the cloud distance, mass, dust temperature, non-thermal velocity dispersion, and virial parameter on the y-axis. Where correlations between the core and cloud properties appear to be present, we conduct a least-squares minimization to a linear relation of $y = ax + b$ to obtain a and b for the plotted variable on the x-axis (x) and y-axis (y). The results of this fitting routine are shown as a grey-dashed line on the panels in Fig. 11. We also determine the Pearson's r value for each parameter set where a fit is possible, which is given in the upper right of the panels. Here, an r of 1(−1) indicates a perfect positive(negative) linear relationship between the variables, whilst an r of 0 indicates no linear relationship between variables.

We first discuss the lack of correlations observed between the cloud and core properties. We find that the non-thermal velocity dispersion and the virial state of the cores do not strongly correlate to any of the compared cloud properties ($|r| < 0.6$). This could be a result of using different molecular lines to determine the dynamical properties for the clouds and cores. The clouds were investigated by Kainulainen & Tan (2013) using ^{13}CO(1−0) emission, whereas here for the cores, we use N_2H^+ emission that has a significantly higher critical density and chemical formation pathway that favours colder, denser gas (Caselli et al. 2002a,b; Hacar & Tafalla 2011; Hacar et al. 2013; Henshaw et al. 2014; Kauffmann et al. 2017; Barnes et al. 2020a). Therefore, the cloud and core scale dynamics could originate from very different density and temperature layers within the molecular cloud. Additionally, it is likely that the clouds contain multiple distinct velocity components that are not resolved within the lower density molecular line tracers such as ^{13}CO(1−0; e.g. Henshaw et al. 2013; Jiménez-Serra et al. 2014; Hacar et al. 2016b; Barnes et al. 2018). If not separated, these would artificially increase the measured velocity dispersion and inferred virial parameters of the clouds (e.g. Henshaw et al. 2014). Alternatively, this lack of correlation could suggest that the cores are dynamically decoupled from their host clouds (e.g. Goodman et al. 1998; Hacar et al. 2016a). In this scenario, we are observing the cores at a stage when a significant fraction of the

turbulence initially inherited from the host molecular cloud has been dissipated, hence the cores are unstable to collapse and are doing so faster than the global cloud. The initial physical properties of these cores could be set by the host molecular cloud, yet their dynamics are now independent of their host environment.

We now discuss the correlations observed between the core and cloud properties. First, we find that the number of cores identified within each cloud, core mass, and radius increase with increasing distance and mass of the cloud. We note that these correlation all have a Pearson's $r > 0.6$, albeit with a strong dependence on the properties determined for Cloud J. There is no physical reason to expect why these properties should scale with increasing cloud distance. This then could be a resolution and sensitivity effect, whereby more massive cores with larger radii are identified within less resolved clouds found at larger distances. Moreover, at larger distances more projected area of the clouds can be mapped for the same angular area on the sky, and therefore there is a higher likelihood of identifying more cores. Alternatively, as the cloud masses are not directly proportional to their distances, and the number of cores, core masses, and radii also appear to scale with cloud mass, there is a different simple conclusion that could be drawn from this result: more massive clouds produce more cores, which also are larger and more massive.

We see that the minimum separation between the cores correlates to the distance and dust temperature of the clouds ($|r| > 0.6$). The correlation to the temperature could be linked to the Jeans fragmentation of the cloud, where higher temperatures produce a larger Jeans length (see equation 7). Assuming the mean temperature of 18 K, and inputting the cloud mass and sizes into equation (7; and a spherical geometry for the density), we calculate λ_J of 0.7 and 3.7 pc for the lowest and largest mass clouds in the sample, respectively. These values are significantly larger than the distribution of observed minimum separations between the cores. There is then the caveat that the observed core spatial distribution is the 2D projection of the true 3D structure of the cloud, and hence could be strongly dependent on the unknown cloud orientation and internal structure (e.g. Henshaw et al. 2016a).

Finally, we find that the number of cores identified within each cloud, core mass, and radius increase with increasing non-thermal velocity dispersion (or sonic Mach number). Such a trend is expected from turbulent star formation theory, where a greater degree of turbulence produces greater contrasts above the mean density, i.e. seen as cores here (see Padoan et al. 2014 for review, also see Palau et al. 2014; Fontani et al. 2018).

4.3.4 From cores (∼0.1 pc scales) to core fragments (∼0.01 pc scales)

We now compare the properties of the cores identified in this work to the properties of their contained smaller scale core fragments.[12] Here, we also calculate the fraction of mass contained within each core fragment to the total mass of the host core, i.e. $f_{\rm mass} = M_{\rm cf}/M_{\rm c}$, where $M_{\rm c}$ is the host core and $M_{\rm cf}$ is the mass of the contained fragment.

Shown in columns from left to right in Fig. 12 are the number, masses, radii, non-thermal velocity dispersion, and virial parameter of the cores identified in this work on the *x*-axis. Shown in rows from top to bottom is how these core properties vary with the mass, radius, and mass fraction contained within the core fragment on the *y*-axis. The points and error bars shown here are the mean and the minimum to maximum value of the fragments contained within each core, respectively. Again here we conduct a least-squares minimization to a linear relation and determine the Pearson's *r*, which is shown in the upper right of the panels in Fig. 12.

We find no significant trends ($|r| > 0.6$) between the core properties and number, masses, or sizes of their contained core fragments. Moreover, we find that none of the core properties has any influence on the fraction of the total core mass contained within each core fragment. Interestingly, we then find that the correlations observed on the cloud to core scales are not present on the core to core fragment scales. Palau et al. (2014) conducted an in-depth study of fragmentation from 0.1 to <0.01 pc scales within a sample of 19 high-mass clumps (also see Palau et al. 2013, 2015, and found tentative trends between host core (clump) and their smaller scale fragment(s) properties, e.g. more fragmentation with increased density. Similarly, Fontani et al. (2018), overall, found weak trends between host clump and core properties from 0.1 to 0.01 pc scales across a sample of 11 high-mass star-forming regions, e.g. more fragmentation with increased turbulence. The reason for the breakdown in the cloud to core correlations on the core to core fragment scales here is then not clear. It could be a result of the different methods and tracers used to determine the core and fragment properties. For example, the comparison of data sets including different spatial filtering, e.g. due to the use of single-dish observations, or differing molecular line to trace dynamics. Alternatively, the differences in trends could be a result of time variability, where a single time snapshot of a population of cores at different evolutionary stages would then naturally produce scatter.

5 CONCLUSIONS

We have presented 3 mm wavelength ALMA observations towards 10 IRDCs. This set of observations currently represents the highest resolution (∼3 arcsec; ∼0.05 pc), highest sensitivity (∼0.15 mJy beam^{-1} full bandwidth or ∼0.2 K per 0.1 km s^{-1} channel) large mosaics (covering parsecs) for a sample of massive molecular clouds. In this work, we conduct an in-depth analysis of the hierarchical structure present within these molecular clouds, and assess the high-mass star-forming potential across fragmentation scales from clouds (∼1 pc), to clumps (∼0.5 pc), to cores (∼0.1 pc), and finally to core fragments (∼0.01 pc). The main conclusions of this work are summarized below.

(i) We identify 96 cores across the 10 clouds within the ALMA continuum maps, which we calculate have masses of $M = 3.4–50.9 M_\odot$ and number densities of $n_{\rm H_2} = 4–12 \times 10^5$ cm^{-3} (ranges are a standard deviation around the median; Section 3.2). We determine their dynamical properties from the brightest velocity component observed within the ALMA N_2H^+ (1−0) emission cubes towards the position of each core. We find sonic (non-thermal) Mach numbers of $\mathcal{M}_{\rm s} = 0.9–2.7$, and virial parameters of $\alpha_{\rm vir} = 0.3–1.3$ (Section 3.3). These results highlight that the cores identified here are dense, gravitationally bound, and dominated by trans-sonic turbulence.

(ii) In addition to the cores identified from the ALMA observations presented here, we include a large sample of cores and clumps from the literature that also covers our 10 cloud sample. The properties of these clump/cores are recalculated using the same assumptions of dust opacity, temperature, and gas-to-dust ratio and definition of

[12]Clouds F and G are not included in this analysis due to the lack of cross-over with the L18 core catalogue, and the catalogue of cores identified in this paper.

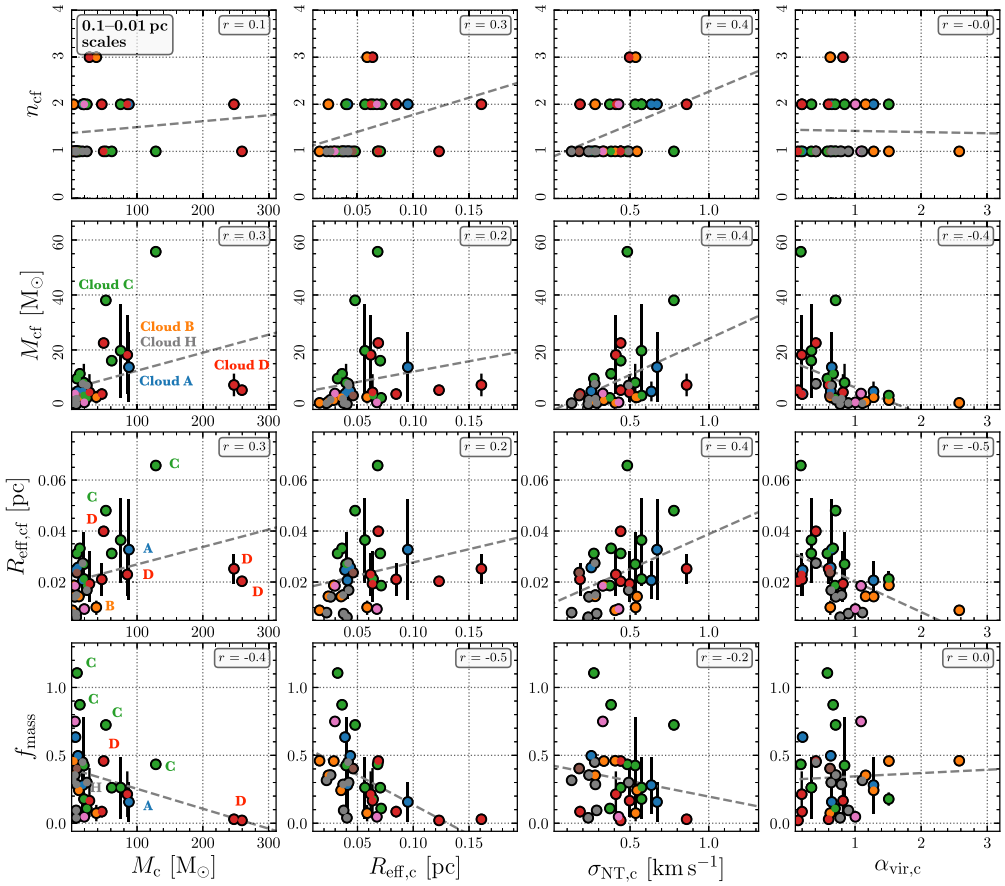

Figure 12. A comparison between the properties of the (∼ 0.1 pc scale) cores identified in this work, and the (∼ 0.01 pc scale) core fragments they contain (see Tables A2 and A3). Shown from left to right in columns is the masses (M_c), radii ($R_{eff,c}$), non-thermal velocity dispersion ($\sigma_{NT,c}$), and virial parameter ($\alpha_{vir,c}$) of the cores identified in this work on the *x*-axis. Shown from top to bottom in rows is the number of core fragments (n_{cf}), mass (M_{cf}), radius ($R_{eff,cf}$), and mass fraction ($f_{mass} = M_{cf}/M_c$) contained within the core fragment on the *y*-axis. The points and error bars shown here are the mean and the minimum to maximum value of the fragments contained within each core, respectively. The grey-dashed lines shows the linear relation ($y = ax + b$) from the least-squares fit of the variables plotted on the *x*- and *y*-axis. The Pearson's-*r* value are given within the upper right of each panel.

radius to produce a homogenized catalogue of core properties. We use the fact that this catalogue has been created using observations that cover the same regions at various spatial resolutions to follow the hierarchical structure within each cloud. To do so, we label which cores are co-spatial, and hence form part of the same fragmentary structure (Section 4.3). We compare this structure for each cloud to mass and density thresholds for massive star formation. We find that from the cloud (∼10 pc) to clump (∼0.5 pc), and to the core (<0.1 pc) scales the fragmentation does not follow a simple power-law relation in the mass–size parameter space, which causes different scales within the same cloud to be classified as high- or low-mass star forming. Caution must then be taken when using density threshold scaling relations to draw conclusions of the high-mass star-forming potential of a core, clump, or cloud across any spatial scale.

(iii) When assessing the simple mass–size relations, we find that on size scales of <0.02 pc (∼2000 au) none of the core fragments appear to contain enough mass to form a high-mass star without additional accretion. However, here we can use the hierarchical structure to determine if any of the larger cores retain enough mass to form a high-mass without further fragmentation. We find that at a size scale of ∼0.1 pc, there is a sample of 19 cores that have masses of >16 $M_\odot$ without further fragmentation. Of these, we find that 6 show no signs of active star formation, whilst 13 have signs of active star formation. These high-mass cores contain transonic non-thermal motions (median $\mathcal{M}_s$ of 2.4), are predominately kinematically sub-virial (median α_{vir} of 0.5), and require moderate magnetic field strengths for support against collapse (median B of 930 μG). We find that the sizes of these cores are broadly comparable to the predictions from the core accretion theory, based on their host cloud properties (McKee & Tan 2003). However, to ultimately test the different theories of HMSF, further investigation is needed to assess if (any) of these fragment further and/or have signs of multiple sites of lower mass star formation (e.g. outflows).

(iv) We investigate what physical and dynamical properties of the cloud (>1 pc scale) are inherited by or influence their smallest scale core fragments (∼0.01 pc scale) populations. We find that more massive, and more turbulent clouds make more ∼0.1 pc scale cores. These ∼0.1 pc scale cores also tend to be more massive within the higher mass, turbulent clouds. We find tentative evidence that these cores then to fragment into more massive ∼0.01 pc scale core fragments.

ACKNOWLEDGEMENTS

We would like to thank the referee for their constructive feedback that helped improve the paper. ATB and FB would like to

acknowledge funding from the European Research Council (ERC) under the European Union's Horizon 2020 research and innovation programme (grant agreement No. 726384/Empire). JEP and PC acknowledge the financial support of the Max Planck Society. IJ-S has received partial support from the Spanish FEDER (project number ESP2017-86582-C4-1-R) and the State Research Agency (AEI; project number PID2019-105552RB-C41). RJP acknowledges support from the Royal Society in the form of a Dorothy Hodgkin Fellowship. ASM research is conducted within the Collaborative Research Centre 956 (sub-project A6), funded by the Deutsche Forschungsgemeinschaft (DFG; project ID 184018867). SF acknowledges the support from the EACOA fellowship from the East Asia Core Observatories Association (EACOA). KW acknowledges support by the National Key Research and Development Program of China (2017YFA0402702, 2019YFA0405100), the National Science Foundation of China (11973013, 11721303), and the starting grant at the Kavli Institute for Astronomy and Astrophysics, Peking University (7101502287). This paper uses the following ALMA data: ADS/JAO.ALMA#2017.1.00687.S and ADS/JAO.ALMA#2018.1.00850.S. We would like to thank Audra Hernandez, Vlas Sokolov, and Andy Pon for their input on the proposal for these AMLA observations. ALMA is a partnership of ESO (representing its member states), NSF (USA) and NINS (Japan), together with NRC (Canada), MOST and ASIAA (Taiwan), and KASI (Republic of Korea), in cooperation with the Republic of Chile. The Joint ALMA Observatory is operated by ESO, AUI/NRAO, and NAOJ.

DATA AVAILABILITY

A full machine-readable version of Tables A1, A2, and A3 is available in the online supplementary of this work. All ALMA observations used within this work are publicly accessible in the ALMA science archive. Additional data products not provided in these tables or available online will be shared on reasonable request to the corresponding author.

REFERENCES

Ballesteros-Paredes J., D'Alessio P., Hartmann L., 2012, MNRAS, 427, 2562
Barnes A. T., Kong S., Tan J. C., Henshaw J. D., Caselli P., Jiménez-Serra I., Fontani F., 2016, MNRAS, 458, 1990
Barnes A. T., Henshaw J. D., Caselli P., Jiménez-Serra I., Tan J. C., Fontani F., Pon A., Ragan S., 2018, MNRAS, 475, 5268
Barnes A. T. et al., 2020a, MNRAS, 497, 1972
Barnes A. T., Longmore S. N., Dale J. E., Krumholz M. R., Kruijssen J. M. D., Bigiel F., 2020b, MNRAS, 498, 4906
Battersby C. et al., 2011, A&A, 535, A128
Bertoldi F., McKee C. F., 1992, ApJ, 395, 140
Bonnell I. A., Bate M. R., Clarke C. J., Pringle J. E., 2001, MNRAS, 323, 785
Bonnell I. A., Vine S. G., Bate M. R., 2004, MNRAS, 349, 735
Butler M. J., Tan J. C., 2009, ApJ, 696, 484
Butler M. J., Tan J. C., 2012, ApJ, 754, 5
Butler M. J., Tan J. C., Kainulainen J., 2014, ApJ, 782, L30
Carey S. J., Clark F. O., Egan M. P., Price S. D., Shipman R. F., Kuchar T. A., 1998, ApJ, 508, 721
Carey S. J. et al., 2009, PASP, 121, 76
Caselli P., Myers P. C., 1995, ApJ, 446, 665
Caselli P., Myers P. C., Thaddeus P., 1995, ApJ, 455, L77 +
Caselli P., Walmsley C. M., Zucconi A., Tafalla M., Dore L., Myers P. C., 2002a, ApJ, 565, 331
Caselli P., Benson P. J., Myers P. C., Tafalla M., 2002b, ApJ, 572, 238
Chen B.-Q. et al., 2020, MNRAS, 493, 351
Cheng Y., Tan J. C., Liu M., Kong S., Lim W., Andersen M., Da Rio N., 2018, ApJ, 853, 160
Chevance M. et al., 2020a, MNRAS, preprint (arXiv:2010.13788)
Chevance M. et al., 2020b, MNRAS, 493, 2872
Churchwell E. et al., 2009, PASP, 121, 213
Cosentino G. et al., 2018, MNRAS, 474, 3760
Cosentino G. et al., 2019, ApJ, 881, L42
Crutcher R. M., Wandelt B., Heiles C., Falgarone E., Troland T. H., 2010, ApJ, 725, 466
Dirienzo W. J., Brogan C., Indebetouw R., Chandler C. J., Friesen R. K., Devine K. E., 2015, AJ, 150, 159
Draine B. T., 2011, Physics of the Interstellar and Intergalactic Medium, Available at: https://press.princeton.edu/books/paperback/9780691122144/physics-of-the-interstellar-and-intergalactic-medium
Dunham M. K., Rosolowsky E. II N. J. E., Cyganowski C., Urquhart J. S., 2011, ApJ, 741, 110
Egan M. P., Shipman R. F., Price S. D., Carey S. J., Clark F. O., Cohen M., 1998, ApJ, 494, L199 +
Elia D. et al., 2017, MNRAS, 471, 100
Feng S., Beuther H., Zhang Q., Henning T., Linz H., Ragan S., Smith R., 2016a, A&A, 592, A21
Feng S., Beuther H., Zhang Q., Liu H. B., Zhang Z., Wang K., Qiu K., 2016b, ApJ, 828, 100
Fontani F., Commerçon B., Giannetti A., Beltrán M. T., Sánchez-Monge Á., Testi L., Brand J., Tan J. C., 2018, A&A, 615, A94
Fontani F. et al., 2021, MNRAS, submitted
Fuller G. A., Myers P. C., 1992, ApJ, 384, 523
Gerner T., Shirley Y., Beuther H., Semenov D., Linz H., Abertsson T., Henning T., 2015, preprint (arXiv:1503.06594)
Ginsburg A., Mirocha J., 2011, Astrophysics Source Code Library, record ascl:1109.001
Goodman A. A., Barranco J. A., Wilner D. J., Heyer M. H., 1998, ApJ, 504, 223
Hacar A., Tafalla M., 2011, A&A, 533, A34
Hacar A., Tafalla M., Kauffmann J., Kovács A., 2013, A&A, 554, A55
Hacar A., Kainulainen J., Tafalla M., Beuther H., Alves J., 2016a, A&A, 587, A97
Hacar A., Alves J., Burkert A., Goldsmith P., 2016b, A&A, 591, A104
Henshaw J. D., Caselli P., Fontani F., Jiménez-Serra I., Tan J. C., Hernandez A. K., 2013, MNRAS, 428, 3425 (Paper IV)
Henshaw J. D., Caselli P., Fontani F., Jiménez-Serra I., Tan J. C., 2014, MNRAS, 440, 2860 (Paper VI)
Henshaw J. D. et al., 2016a, MNRAS, 463, 146 (H16)
Henshaw J. D. et al., 2016b, MNRAS, 457, 2675
Henshaw J. D. et al., 2017, MNRAS, 464, L31 (H17)
Henshaw J. D. et al., 2019, MNRAS, 485, 2457
Hernandez A. K., Tan J. C., Caselli P., Butler M. J., Jiménez-Serra I., Fontani F., Barnes P., 2011, ApJ, 738, 11 (Paper II)
Jackson J. M. et al., 2006, ApJS, 163, 145
Jeans J. H., 1902, Phil. Trans. R. Soc. A, 199, 1
Jiménez-Serra I., Caselli P., Fontani F., Tan J. C., Henshaw J. D., Kainulainen J., Hernandez A. K., 2014, MNRAS, 439, 1996 (Paper V)
Kainulainen J., Tan J. C., 2013, A&A, 549, A53
Kainulainen J., Beuther H., Henning T., Plume R., 2009, A&A, 508, L35
Kauffmann J., Pillai T., 2010, ApJ, 723, L7
Kauffmann J., Bertoldi F., Bourke T. L., Evans N. J., II, Lee C. W., 2008, A&A, 487, 993
Kauffmann J., Pillai T., Shetty R., Myers P. C., Goodman A. A., 2010a, ApJ, 712, 1137
Kauffmann J., Pillai T., Shetty R., Myers P. C., Goodman A. A., 2010b, ApJ, 716, 433
Kauffmann J., Pillai T., Zhang Q., 2013, ApJ, 765, L35
Kauffmann J., Goldsmith P. F., Melnick G., Tolls V., Guzman A., Menten K. M., 2017, A&A, 605, L5
Kepley A. A., Tsutsumi T., Brogan C. L., Indebetouw R., Yoon I., Mason B., Meyer J. D., 2020, PASP, 132, 024505
Kong S. et al., 2016, ApJ, 821, 94

Kong S., Tan J. C., Caselli P., Fontani F., Liu M., Butler M. J., 2017, ApJ, 834, 193
Kong S., Tan J. C., Arce H. G., Caselli P., Fontani F., Butler M. J., 2018, ApJ, 855, L25
Kong S., Arce H. G., Maureira M. J., Caselli P., Tan J. C., Fontani F., 2019, ApJ, 874, 104
Kruijssen J. M. D. et al., 2019, Nature, 569, 519
Krumholz M. R., McKee C. F., 2008, Nature, 451, 1082
Lada C. J., Dame T. M., 2020, ApJ, 898, 3
Larson R. B., 1981, MNRAS, 194, 809
Lim W., Tan J. C., Kainulainen J., Ma B., Butler M. J., 2016, ApJ, 829, L19
Lindner R. R. et al., 2015, AJ, 149, 138
Liu T. et al., 2018a, ApJ, 859, 151
Liu M., Tan J. C., Cheng Y., Kong S., 2018b, ApJ, 862, 105 (L18)
Liu M. et al., 2020a, ApJ, 904, 75
Liu J., Zhang Q., Qiu K., Baobab Liu H., Pillai T., Miquel Girart J., Li Z.-Y., Wang K., 2020b, ApJ, 895, 142
Longmore S. N. et al., 2012, ApJ, 746, 117
Marsh K. A., Ragan S. E., Whitworth A. P., Clark P. C., 2016, MNRAS, 461, L16
Marsh K. A. et al., 2017, MNRAS, 471, 2730
Marton G. et al., 2017, preprint (arXiv:1705.05693)
McKee C. F., Ostriker E. C., 2007, ARA&A, 45, 565
McKee C. F., Tan J. C., 2003, ApJ, 585, 850
McMullin J. P., Waters B., Schiebel D., Young W., Golap K., 2007, in Shaw R. A., Hill F., Bell D. J., eds, ASP Conf. Ser., Vol. 376, Astronomical Data Analysis Software and Systems XVI. Astron. Soc. Pac., San Fransisco, p. 127
Miettinen O., Hennemann M., Linz H., 2011, A&A, 534, A134
Molinari S. et al., 2016, A&A, 591, A149
Motte F., Bontemps S., Louvet F., 2018, ARA&A, 56, 41
Nguyen Luong Q. et al., 2011, A&A, 535, A76
Ossenkopf V., Henning T., 1994, A&A, 291, 943
Padoan P., Federrath C., Chabrier G., Evans N. J., II, Johnstone D., Jørgensen J. K., McKee C. F., Nordlund Å., 2014, in Beuther H., Klessen R. S., Dullemond C. P., Henning T., eds, Protostars and Planets VI, University of Arizona Press. p. 77
Padoan P., Pan L., Juvela M., Haugbølle T., Nordlund Å., 2020, ApJ, 900, 82
Pagani L., Daniel F., Dubernet M., 2009, A&A, 494, 719
Palau A. et al., 2013, ApJ, 762, 120
Palau A. et al., 2014, ApJ, 785, 42
Palau A. et al., 2015, MNRAS, 453, 3785
Pérault M. et al., 1996, A&A, 315, L165
Peretto N., Fuller G. A., 2010, ApJ, 723, 555
Peretto N. et al., 2010, A&A, 518, L98
Peretto N. et al., 2013, A&A, 555, A112
Peretto N. et al., 2020, MNRAS, 496, 3482
Pety J. et al., 2017, A&A, 599, A98
Pillai T., Wyrowski F., Carey S. J., Menten K. M., 2006, A&A, 450, 569
Pillai T., Kauffmann J., Wyrowski F., Hatchell J., Gibb A. G., Thompson M. A., 2011, A&A, 530, A118
Pillai T., Kauffmann J., Tan J. C., Goldsmith P. F., Carey S. J., Menten K. M., 2015, ApJ, 799, 74
Pillai T., Kauffmann J., Wiesemeyer H., Menten K. M., 2016, A&A, 591, A19
Pineda J. E. et al., 2015, Nature, 518, 213
Ragan S. E., Bergin E. A., Wilner D., 2011, ApJ, 736, 163
Ragan S. E., Heitsch F., Bergin E. A., Wilner D., 2012, ApJ, 746, 174
Rathborne J. M., Jackson J. M., Simon R., 2006, ApJ, 641, 389
Riener M., Kainulainen J., Henshaw J. D., Orkisz J. H., Murray C. E., Beuther H., 2019, A&A, 628, A78
Rigby A. J. et al., 2021, MNRAS, 502, 4576
Rosolowsky E. W., Pineda J. E., Kauffmann J., Goodman A. A., 2008, ApJ, 679, 1338
Sadaghiani M. et al., 2020, A&A, 635, A2
Sánchez-Monge Á. et al., 2013, MNRAS, 432, 3288
Sanhueza P., Jackson J. M., Zhang Q., Guzmán A. E., Lu X., Stephens I. W., Wang K., Tatematsu K., 2017, ApJ, 841, 97
Simon R., Jackson J. M., Rathborne J. M., Chambers E. T., 2006a, ApJ, 639, 227
Simon R., Rathborne J. M., Shah R. Y., Jackson J. M., Chambers E. T., 2006b, ApJ, 653, 1325
Soam A. et al., 2019, ApJ, 883, 95
Sokolov V. et al., 2017, A&A, 606, A133
Tan J. C., Kong S., Butler M. J., Caselli P., Fontani F., 2013, ApJ, 779, 96
Tan J. C., Beltrán M. T., Caselli P., Fontani F., Fuente A., Krumholz M. R., McKee C. F., Stolte A., 2014, in Beuther H., Klessen R. S., Dullemond C. P., Henning T., eds, Protostars and Planets VI, University of Arizona Press, p. 149
Tanaka K. E. I., Tan J. C., Zhang Y., 2017, ApJ, 835, 32
Tang Y.-W., Koch P. M., Peretto N., Novak G., Duarte-Cabral A., Chapman N. L., Hsieh P.-Y., Yen H.-W., 2019, ApJ, 878, 10
Terebey S., Chandler C. J., Andre P., 1993, ApJ, 414, 759
Vasyunina T., Linz H., Henning T., Stecklum B., Klose S., Nyman L.-Å., 2009, A&A, 499, 149
Vázquez-Semadeni E., Palau A., Ballesteros-Paredes J., Gómez G. C., Zamora-Avilés M., 2019, MNRAS, 490, 3061
Williams J. P., Blitz L., McKee C. F., 2000, Protostars and Planets IV, University of Arizona Press. p. 97
Zhang Q., Wang K., Lu X., Jiménez-Serra I., 2015, ApJ, 804, 141
Zhang C.-P., Yuan J.-H., Li G.-X., Zhou J.-J., Wang J.-J., 2017, A&A, 598, A76
Zinnecker H., Yorke H. W., 2007, ARA&A, 45, 481

SUPPORTING INFORMATION

Supplementary data are available at *MNRAS* online.

Appendix A. Observational properties of the core population (Sections 3.1, 3.3, and 4.3).
Appendix B. Physical properties of the core population (Sections 3.2 and 3.3).
Appendix C. Properties of the homogenized literature core sample (Section 4.1).

Please note: Oxford University Press is not responsible for the content or functionality of any supporting materials supplied by the authors. Any queries (other than missing material) should be directed to the corresponding author for the article.

APPENDIX A: LITERATURE CORES AND FRAGMENTATION ANALYSIS

In the section, we present the complete core and homogenized literature core catalogues used throughout this work, which can be found in full, machine-readable format online. Moreover, we present the fragmentation structure determined within each cloud, which has been summarized in Fig. A1 of the main text (Section 4.3).

Table A1 presents the observed properties of each core determined from the the dendrogram analysis (Section 3.1), their spectroscopic properties determined from the N_2H^+ Gaussian fits (Section 3.3), and host millimetre (MM) core (Rathborne et al. 2006). Table A2 presents the physical properties of the identified cores (Sections 3.2 and 3.3). Table A3 presents the literature core catalogue (Rathborne et al. 2006; Henshaw et al. 2016a, 2017; Liu et al. 2018b). Here, the spatial (effective) radii and masses of each core have been re-calculated from the observed angular (effective) radii and continuum fluxes using the same set of assumptions for the dust opacity, dust-to-gas ratio, and dust temperature (Section 4.1).

Table A1. Observational properties of the core population (Sections 3.1, 3.3, and 4.3). Shown in columns are the results from the dendrogram analysis of the core ID and name, the host cloud, the centre RA and Dec., the effective radius ($R_{\rm eff}$ in units of arcsec), the total continuum flux density (S_ν) and background-subtracted flux density ($S_\nu^{\rm b}$), and the peak continuum intensity [I_ν(max)]. Also given are the results of the N_2H^+ Gaussian fits of peak brightness temperature ($T_{\rm max}$), centroid velocity (v_0) and velocity dispersion ($\sigma_{\rm v}$). We show the millimetre (MM) core in which each core is contained (Rathborne et al. 2006). Finally, we show if the core contains an embedded (*Spitzer* or *Herschel* 70 μm) infrared point source, and the flux density of any associated 70 μm point sources ($S_{70\,\mu{\rm m}}$; Molinari et al. 2016; Marton et al. 2017).

ID	Name	Cloud	RA (J2000) °	Dec. (J2000) °	$R_{\rm eff}$ (arcsec)	S_ν (mJy)	$S_\nu^{\rm b}$ (mJy)	I_ν(max) (mJy)	$T_{\rm max}$ (K)	v_0 (km s^{-1})	$\sigma_{\rm v}$ (km s^{-1})	MM core (Jy)	SF	$S_{70\,\mu{\rm m}}$
1	A1c1/2	cloudA	276.564	−12.694	4.1	3.97	2.28	2.00	2.1	64.7	0.7	MM4	y	-
2	A1c3	cloudA	276.566	−12.692	2.3	0.84	0.34	0.72	2.0	65.7	0.3	MM4	n	-
3	A1c4	cloudA	276.564	−12.692	1.8	0.41	0.06	0.46	1.9	65.0	0.5	MM4	y	-
4	A1c5	cloudA	276.569	−12.690	2.2	0.59	0.17	0.48	2.4	66.3	0.4	MM4	y	3.05
5	A2c2	cloudA	276.580	−12.688	1.9	0.45	0.17	0.58	2.4	66.3	0.4	MM6	n	-
...	...	...	...	...	...	...	...	...	...	...	...	...		

Note. The full, machine-readable version of this Table can be obtained from the supplementary online material.

Table A2. Physical properties of the core population (Sections 3.2 and 3.3). Shown in columns are the core name (Table A1), the effective radius (in units of parsec; $R_{\rm eff}$), the minimum separation or nearest neighbour distance ($S_{\rm min}$), the mean dust temperature ($T_{\rm dust}$), the mass determined using the mean dust temperature (M), the background-subtracted mass using the mean dust temperature ($M^{\rm b}$), the mass determined using a constant temperature of 18 K ($M_{\rm 18K}$), the mass determined from the near- and mid- infrared extinction maps ($M_{\rm ext}$; Kainulainen & Tan 2013), the mass estimates using a temperature determined from 70 μm emission ($M_{70\,\mu{\rm m}}$), the mean density ($n_{\rm H_2}$), the free-fall time ($t_{\rm ff}$), virial parameter ($\alpha_{\rm vir}$), background-subtracted virial parameter ($\alpha_{\rm vir}^{\rm b}$), the non-thermal velocity dispersion ($\sigma_{\rm NT}$), the sonic Mach number ($\mathcal{M}_{\rm s}$), the Alfvén Mach number ($\mathcal{M}_{\rm A}$) and magnetic field strength to reach gravitational equilibrium (B; Section 3.4.3).

Name	$R_{\rm eff}$ (pc)	$S_{\rm min}$ (pc)	$T_{\rm dust}$ (K)	M ($M_\odot$)	$M^{\rm b}$ ($M_\odot$)	$M_{\rm 18K}$ ($M_\odot$)	$M_{\rm ext}$ ($M_\odot$)	$M_{70\,\mu{\rm m}}$ ($M_\odot$)	$n_{\rm H_2}$ (10^5 cm^3)	$t_{\rm ff}$ (10^4 yr)	$\alpha_{\rm vir}$	$\alpha_{\rm vir}^{\rm b}$	$\sigma_{\rm NT}$ (km s^{-1})	$\mathcal{M}_{\rm s}$	$\mathcal{M}_{\rm A}$	B (μG)
A1c1/2	0.095	0.2	17.6	87.6	50.2	85.3	45.0	–	3.5	5.2	0.6	1.1	0.7	2.8	6.1	665
A1c3	0.055	0.2	17.4	18.6	7.7	17.9	14.3	–	4.0	4.9	0.2	0.5	0.1	0.3	4.3	492
A1c4	0.043	0.2	17.5	9.1	1.4	8.8	4.2	–	4.1	4.8	1.3	8.3	0.4	1.7	2.1	251
A1c5	0.051	0.3	18.0	12.6	3.5	12.6	–	8.3	3.2	5.4	0.6	2.1	0.2	1.0	3.2	335
A2c2	0.044	0.1	17.3	10.1	3.7	9.7	9.9	–	4.2	4.7	0.6	1.7	0.3	1.1	3.1	368
...	...	...	...	...	...	...	...	...	...	...	...	...	...	...		

Note. The full, machine-readable version of this Table can be obtained from the supplementary online material. Were applicable, the online table also includes all the properties determined with and without background subtraction for the flux density, and using the measured mean and constant 18 K dust temperature.

Table A3. Properties of the homogenized literature core sample (Section 4.1). Shown in columns is the host cloud name and ID, the centre RA and Dec., the effective radius in arcsec and parsec ($R_{\rm eff}$), the total flux density at the observed frequency (S_λ), the mass assuming a constant temperature of 18 K, the wavelength of the observations (see Table 3), and the reference (Rathborne et al. 2006; Henshaw et al. 2016a, 2017; Liu et al. 2018b).

Cloud	ID	Core	RA (°)	Dec. (°)	$R_{\rm eff}$ (arcsec)	$R_{\rm eff}$ (pc)	S_λ (Jy)	$M_{\rm 18K}$ ($M_\odot$)	λ (mm)	Reference
cloudA	G018.82-00.28	A3c4	276.5900	−12.6863	0.72	0.017	3.79	3.09	1.3	Liu et al. (2018b)
cloudA	G018.82-00.28	MM5	276.5875	−12.6864	15.00	0.320	234.60	144.62	1.3	Rathborne et al. (2006)
cloudA	G018.82-00.28	A1c3	276.5662	−12.6921	2.34	0.055	0.84	17.95	3.0	This work
cloudA	G018.82-00.28	A2c1	276.5777	−12.6883	1.06	0.025	4.91	4.01	1.3	Liu et al. (2018b)
cloudA	G018.82-00.28	A1c2	276.5640	−12.6937	2.26	0.052	32.38	26.43	1.3	Liu et al. (2018b)
cloudA	G018.82-00.28	A1c5	276.5692	−12.6900	2.20	0.051	0.59	12.61	3.0	This work
...	...	...	...	...	...	...	...	...	...	

Note. The full, machine-readable version of this Table can be obtained from the supplementary online material. This is a literature compilation, please ensure to cite each individual study when making use of the contents of this table.

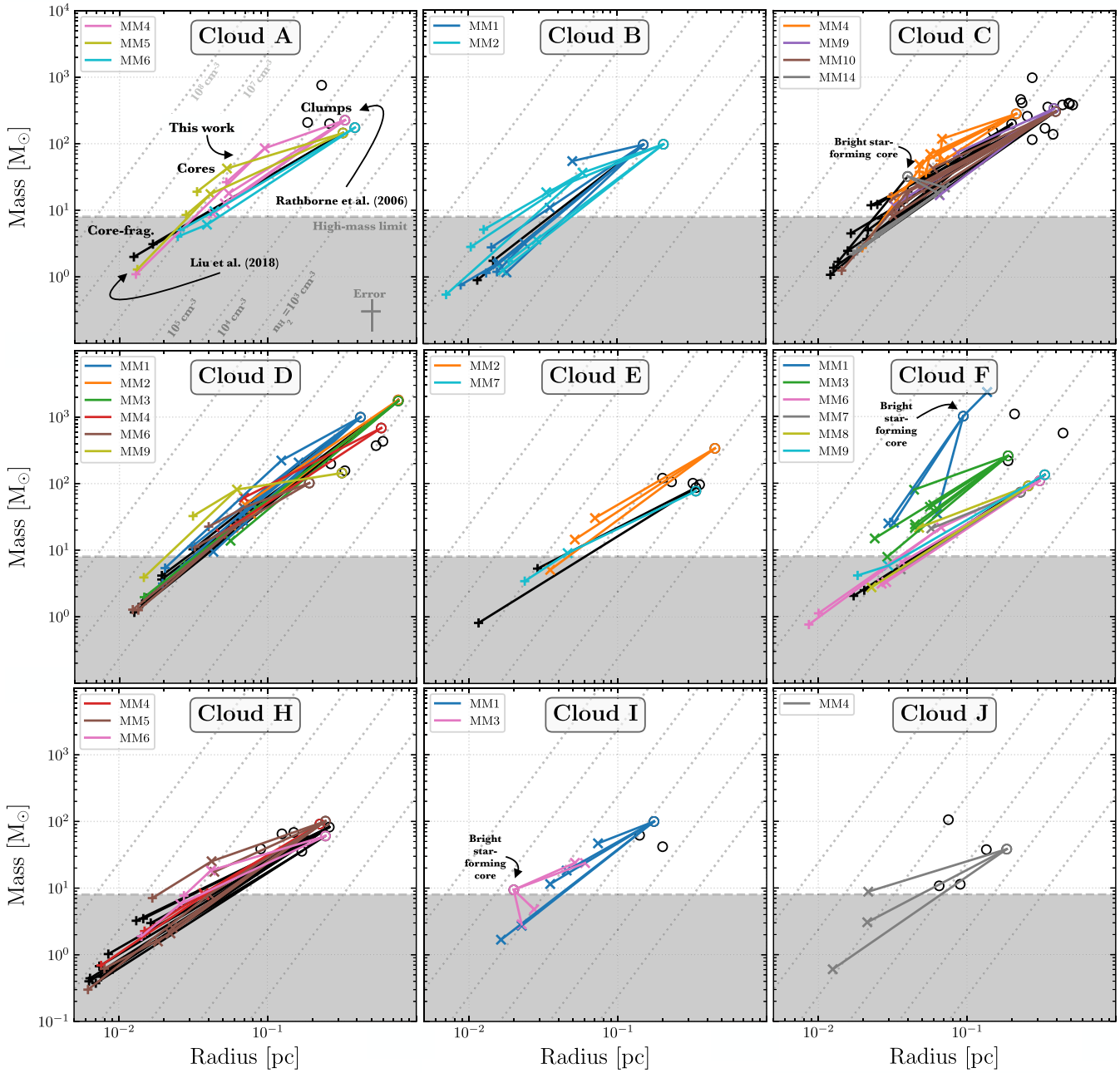

Figure A1. Mass fragmentation of the cores within each IRDC as a function of the size-scale. The circles, the crosses, and the plus sign markers represent the cores from the homogenized sample identified by Rathborne et al. (2006); this work and Liu et al. (2018b; Section 4.1). The straight lines connect the symbols for each core and the larger, host core of which it is a part [Section 4.3. The lines and symbols have been coloured by host 'MM' Rathborne et al. (2006) core, as indicated in the legend located in the upper left (see Table A3)]. Also highlighted with labels are the clumps associated within bright star-forming regions, which limits the mass determination from the lower resolution observations from Rathborne et al. (2006). The resultant large uncertainty on the mass estimate can cause these Rathborne et al. (2006) structures to appear to have masses smaller than is determined in this work. Their hierarchical structure should therefore be taken with caution. Cloud G is not shown due to the lack of continuum cores determined in the 3 mm ALMA continuum observations presented as part of this work (Section 3.1). The shaded region shows the 8 $M_\odot$ mass threshold for a high-mass star. In the lower right corner of the upper left-hand panel, we show a representative uncertainty range ∼15 and ∼50 per cent on the radius and mass, respectively.

APPENDIX B: COMPARISON OF FEATHERING AND UV-COMBINATION

The combination of multiple data sets is typical for interferometric observations, where the range of recoverable spatial scales is limited by the baselines included in each observation. There is still, however, much debate within the literature for the best practices for this combination, and particularly for the case where single-dish observations are used with interferometric data sets to recover the zero-spacing. Throughout this work, we use ALMA observations taken with both the 12 and 7 m arrays, which were reduced using the CASA-PIPELINE (version: 5.4.0-70) and combined using the FEATHER (CASA version: 4.7.0). For the follow-up work investigating the nitrogen fractionation, we have also combined the single-dish

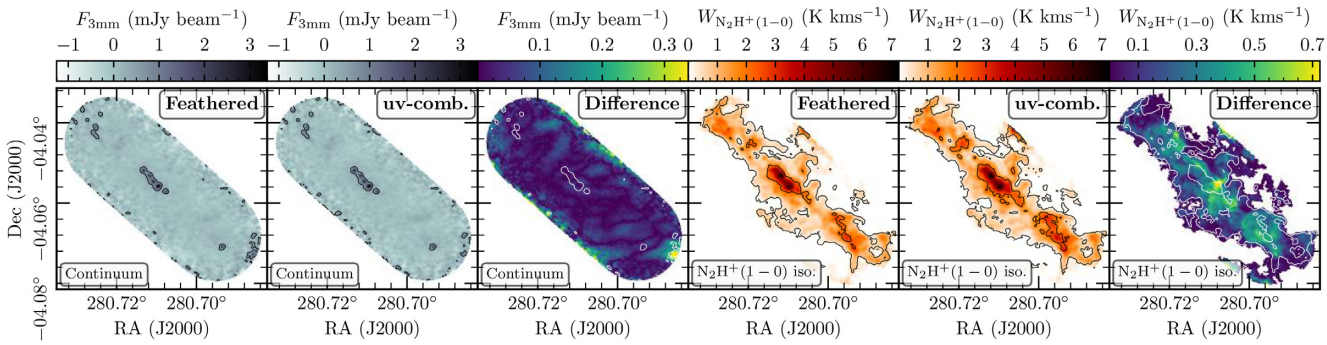

Figure B1. A comparison between the images produced when feathering the pipeline imaged 12 and 7 m data sets, and when imaging the 12 and 7 m data sets together in the *uv*-plane with the clean function for Cloud C (see Fig. 2). The left two panels show the feathered, and *uv*-combined, cleaned continuum maps, overlaid with a solid black contour of the 0.48 mJy beam^{-1}. The centre left shows a map of the difference between these two continuum images. The fourth and fifth panels show the feathered and cleaned N_2H^+ (1−0) integrated intensity maps. In both cases the integrated intensity has been determined over the isolated hyperfine component of N_2H^+ (1−0), using the same mask and velocity range. Overlaid are the solid black contours at signal-to-noise levels of 3σ and 5σ. The rightmost panel shows the difference between these N_2H^+ (1−0) integrated intensity maps. Note that the feathered and cleaned continuum and integrated intensity maps have the same colour scale, and the respective difference map has a range of 1/10 this colour scale.

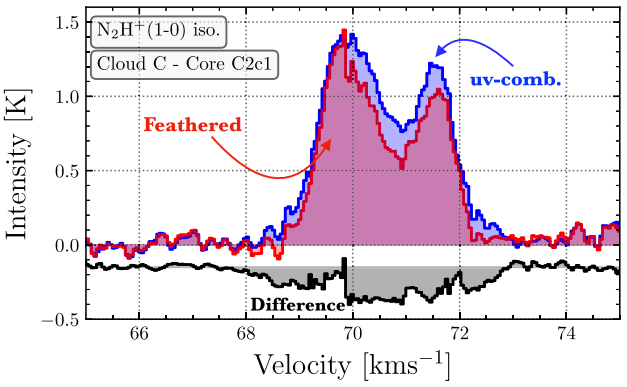

Figure B2. A comparison between the N_2H^+ (1−0) cubes produced when feathering the pipeline imaged 12 and 7 m data sets, and when imaging the 12 and 7 m data sets together in the *uv*-plane with the clean function for Cloud C (see Fig. 2). Shown in blue and red are mean spectra of the isolated hyperfine component of N_2H^+ (1−0) across the core C2c1. Shown in black and centred on −0.15 K is the difference between these two spectra.

observations with the 12 and 7 m images using the same procedure (Fontani et al. 2021). We chose to feather the images produced directly by the pipeline for convenience. However, an alternative, commonly used approach, is to combine the array configurations in the *uv*-plane and to then image them together using the, e.g. CLEAN function.

In light of the above, in this section, we conduct a comparison between the continuum map and N_2H^+ (1−0) cube within Cloud C produced by combining the 12 and 7 m data sets in the FEATHER and TCLEAN functions. First, for the continuum, we use the calibrated measurement sets produced by the pipeline that have not been continuum subtracted and use the line-free parts of the bandwidth identified from the HIf_FINDCONT task in the CASA-PIPELINE. When imaging with TCLEAN (version: 5.6.0), we use natural weighting, a multiterm (multiscale) multifrequency synthesis deconvolver (MTMFS option), and set a high number of iterations to achieve a noise threshold of 0.5 mJy beam^{-1} within a mask that is automatically determined after each minor cycle (see the AUTO-MULTITHRESH option for the USEMASK parameter in TCLEAN; Kepley et al. 2020). Secondly, for the N_2H^+ (1−0) cubes, we use the continuum-subtracted measurement set produced by the pipeline. When imaging, we again use natural weighting, a multiscale deconvolver (MULTISCALE option), set a high number of interactions to achieve a noise threshold of 21 mJy per beam per channel within an automatically determined mask.

Fig. B1 shows the feathered and uv-combined, cleaned continuum maps and N_2H^+ (1−0) integrated intensity maps for Cloud C, where the integrated intensity has been determined using the same mask and velocity range for both cubes. Here, we match the colour bar scales for both maps for ease of comparison, and overlay contours at signal-to-noise levels of 3σ and 5σ (see table 2). We see here that both qualitatively and quantitatively the maps produced with the FEATHER and TCLEAN functions are very similar, and only minor differences can be seen on close inspection. To further quantify this, in Fig. B1 we also present maps of the absolute difference between the feathered and cleaned images. We find absolute differences of up to 10 per cent between the two methods; note the colour scale range used to show the difference maps is 1/10 of the maximum of the cleaned and feathered maps. This difference is, however, small compared to the underlying systematic uncertainties inherent in the physical properties that these maps are used to calculate within this work (e.g. for the mass, where the combined uncertainty from the temperature and distance will be factors of a few higher).

Along with examining the 2D distributions for N_2H^+ (1−0), we can also use the cubes to compare the FEATHER and TCLEAN 12 and 7 m combination for each velocity slice. Fig. B2 shows the spectra of the isolated component of N_2H^+ (1−0) averaged over the core C2c1, which is the closest core to the largest difference in the N_2H^+ (1−0) integrated intensity maps (Fig. B1). These spectra both show profiles that contain only two Gaussian profiles, which are separated by ∼2 km s^{-1}. However, we see that the feathered spectrum has systematically lower intensities than the cleaned spectrum, which is highlighted by the difference profile. Where present, we find that this difference ranges from 20 to 50 per cent of the feathered spectrum intensity, and is therefore larger than observed within the integrated intensity map. That said, it is worth keeping in mind that in this work we only use the linewidth for the dynamical analysis of the cores, which will be less sensitive to systematic differences within the intensity.

In summary, in this section, we find that there are some differences between the map produced when feathering the pipeline imaged 12 and 7 m data sets, and when imaging the 12 and 7 m data sets together

in the clean function. These differences are of the order 10 per cent, but can be more substantial when inspecting the individual slices of a datacube. However, ultimately, the differences between the two methods are small compared to the systematic uncertainty inherent within the physical properties calculated within this work. The analysis presented here then validates our choice of using the feathered, pipeline reduced images, throughout this work.

This paper has been typeset from a TEX/LATEX file prepared by the author.